

3 X-RAY SPECTRAL STATE EVOLUTION IN IGR J17091–3624 AND COMPARISON OF ITS HEARTBEAT
4 OSCILLATION PROPERTIES WITH THOSE OF GRS 1915+105

5 MAYUKH PAHARI¹, J S YADAV¹ AND SUDIP BHATTACHARYYA¹

6 ¹ Tata Institute of Fundamental Research, Homi Bhabha Road, Mumbai, India; mp@tifr.res.in
7

Draft version August 16, 2018

8 ABSTRACT

9 In this work, we study the X-ray timing and spectral evolution of the transient low mass X-ray
10 binary IGR J17091–3624 during first 66 days of its 2011 outburst. We present results obtained from
11 observations with two instruments, *Rossi X-ray Timing Explorer (RXTE)* Proportional Counter Array
12 (PCA) and *SWIFT* X-ray telescope (XRT), between 09 February, 2011 and 15 April, 2011. Using
13 quasi-periodic oscillation classifications, power density spectrum characteristics, time-lag behavior and
14 energy spectral properties, we determine source states and their transitions at different times of the
15 outburst. During the first part of the evolution, the source followed trends usually observed from
16 transient black hole X-ray binaries (BHXBs). Interestingly, a gradual transition is observed in IGR
17 J17091–3624 from the low-variability SIMS, commonly seen in BHXBs, to a high-variability state
18 with regular, repetitive and structured pulsations, seen only from GRS 1915+105 (also known as ‘ ρ ’
19 class variability/‘heartbeat’ oscillations). We study the time evolution of characteristic time-scale,
20 quality factor and rms amplitude of heartbeat oscillations in IGR J17091–3624. We also present a
21 detailed comparison of the timing and spectral properties of heartbeat oscillations and their evolution
22 in IGR J17091–3624 and GRS 1915+105.

23 *Subject headings:* accretion, accretion disks — black hole physics — X-rays: binaries — X-rays:
24 individual: (IGR J17091–3624, GRS 1915+105)

25 1. INTRODUCTION

26 IGR J17091–3624 was detected as a bright, vari-
27 able, transient source with flaring activity in Octo-
28 ber 1994 (Mir/KVANT/TTM), September 1996 (Bep-
29 poSAX/WFC), September 2001 (BeppoSAX/WFC;
30 In’t Zand et al. (2003)), April 2003 (INTEGRAL/IBIS;
31 Kuulkers et al. (2003)), and July 2007 (Capitanio et al.
32 2009). In April 2003, IBIS, the Gamma-ray imager
33 on board the *INTEGRAL* satellite detected the tran-
34 sient X-ray binary IGR J17091–3624 at the posi-
35 tion of $17^h09.1^m$ (R.A. (J2000.0)), $-36^\circ24.63'$ (decli-
36 nation (J2000.0)) while monitoring the Galactic centre
37 (Kuulkers et al. 2003). A transition between soft and
38 hard states and the presence of a blackbody compo-
39 nent during source softening were observed during a joint
40 spectral analysis of *INTEGRAL*/IBIS and *RXTE*/PCA
41 data by Capitanio et al. (2006). They found that the dif-
42 ferent spectral states, their transitions, and time variabil-
43 ity of the source were similar to those of the black hole
44 candidate H1743–322. The approach which is commonly used to define the spec-
45 tral states of a source during an outburst evolution is
46 based on energy spectral properties as well as power den-
47 sity spectral (PDS) properties including low-frequency
48 quasi-periodic oscillations (LF QPOs) features and clas-
49 sifications (Fender, Belloni & Gallo 2004). Depending
50 on QPO frequency, coherence and strength, three main
51 types of LF QPOs are observed in BHXBs - type-A
52 (weak (with few percent of rms amplitude) and broad
53 (q-factor ≤ 3) QPO around 7–9 Hz; (Casella et al.
54 2005; Soleri et al. 2008)), type-B (relatively strong (~ 4 -
55 7% rms amplitude) and relatively narrow (q-factor
56 ~ 5 –7) QPO around 5–7 Hz appeared with a weak red
57

58 noise (Casella et al. 2005; Soleri et al. 2008)) and type-
59 C (strong (up to $\sim 21\%$ rms amplitude) and narrow (q-
60 factor ~ 5 –12) features with the variable centroid fre-
61 quency between 0.1–15 Hz, superposed on a strong flat-
62 top noise (Casella et al. 2005; Soleri et al. 2008)). Type-
63 B QPOs are generally associated with relatively soft
64 state or soft intermediate state (SIMS) (Belloni et al.
65 2005; Fender, Belloni & Gallo 2004) while type-C QPOs
66 carry the signature of the hard intermediate state
67 (HIMS; (Belloni et al. 2005; Fender, Belloni & Gallo
68 2004)). Along with different types of QPOs, one im-
69 portant difference, which has also been used in this work
70 to distinguish the HIMS from the SIMS is that type-
71 B QPOs always show hard lag (hard photons lag soft
72 photons) at the fundamental QPO frequency between
73 5–7 Hz, but a type-C QPO, if detected in the fre-
74 quency range 5–7 Hz during the HIMS, always shows soft
75 lag at the fundamental QPO frequency (Casella et al.
76 2005). The low/hard state (LS) is usually characterized
77 by strong band-limited noise where noise component can
78 be decomposed into a few broad Lorentzian components
79 (Belloni et al. 2005).

80 Lutovinov et al. (2003) found that the PDS of IGR
81 J17091–3624 could be well described with the standard
82 model of band-limited noise with the break frequency of
83 0.31 ± 0.04 Hz. They fitted the energy spectrum with the
84 power-law model having the power-law index of $1.43 \pm$
85 0.03 . These timing and spectral properties are commonly
86 observed in the LS of BHXBs (Sunyaev & Revnivtsev
87 2000). Using combined *RXTE*/PCA and *INTE-*
88 *GRAL*/IBIS data, Capitanio et al. (2006) showed that
89 a single thermal Comptonization component (compTT in
90 XSpec) or saturated Comptonization (compST in XSpec)
91 or the combination of soft multi-color disk blackbody and

hard power-law (diskbb+powerlaw) are good description of the X-ray spectra of IGR J17091–3624. However, they noticed that the model derived electron temperature was ~ 20 keV, which was less than typical electron temperature of black hole X-ray binaries (~ 50 -100 keV; Zdziarski & Gierlinski (2004)). *SWIFT*/XRT observations of IGR J17091–3624 during the outburst in 2007 revealed another state transition from hard to soft, and refined the X-ray position of this source, which is consistent with the position of the infra-red counterpart observed with the ESO *New Technology Telescope* (NTT) (Chaty et al. 2008) as well as compact radio counterpart in the *VLA* archived data (Capitanio et al. 2009).

The renewed activity of the source was first detected with the *SWIFT*/BAT when the hard X-ray flux (15.0-60.0 keV) increases up to 60 mCrab on 03 February, 2011 (Krimm et al. 2011a). Later using the *SWIFT*/XRT observation, Krimm & Kennea (2011b) confirmed that the outburst occurred in the source IGR J17091–3624, and not in IGR J17098–3628, which is also an X-ray transient 9.6' away from IGR J17091–3624. The *INTEGRAL*/IBIS also detects the source simultaneously with the *SWIFT*/XRT (Del Santo et al. 2011). The preliminary spectral data during the recent outburst of IGR J17091–3624 in 2011 showed that a soft spectral component is necessary to describe the spectrum along with the hard power-law component (Del Santo et al. 2011). Later using the data from IBIS/ISGRI imager and the JEM-X telescope on board the *INTEGRAL* satellite on 7–8 February, 2011, Capitanio et al. (2011) described the combined ISGRI and JEMX2 spectrum (5.0-300.0 keV) with a power law having the high energy cut-off at 110_{-27}^{+47} keV. In spite of several efforts, little is known about the compact nature of this source or the nature of its binary companion (but see Bodagheer et al. (2012)).

From the beginning of *RXTE*/PCA observations on 9 February, 2011, several rich features in timing and spectral domain of the source have been noticed. QPOs at 94 ± 3 mHz and $0.105_{-0.003}^{+0.004}$ Hz with a quality factor of ~ 9.1 and ~ 7.4 respectively, were reported using *RXTE*/PCA observations on 9, 10, 11 and 12 February, 2011 (Rodriguez et al. 2011a) although a source contamination problem exists with the *RXTE* data during this period. Apart from this, fast QPO evolution (Shaposhnikov 2011), 10 mHz QPOs (Altamirano et al. 2011a) and evolving power density spectrum with multiple peaks (Pahari et al. 2011b) were also noticed. High frequency QPO at 66 Hz (Altamirano & Belloni 2012b) was detected with the significance of 8.5σ . Interestingly, a quasi-regular oscillation in the light curve of IGR J17091–3624 is noticed which is very similar to the ' ρ ' class variability seen only in the light curve of the Galactic micro-quasar GRS 1915+105 (Altamirano et al. 2011b). Later, Altamirano et al. (2011c) claimed a few more variabilities similar to those found in GRS 1915+105. Two new variabilities, which are unique to IGR J17091–3624, were reported by Pahari et al. (2011a). Using Chandra spectroscopy of IGR J17091–3624 during soft, disk-dominated state, King et al. (2012) showed that accretion disk wind is anti-correlated with relativistic jets. This disk wind was observed to be highly ionized, dense, and had typical blue-shift of ~ 9300 km/s, or less projected along our line

of sight. Dips in the X-ray intensity, which are observed in the κ/λ class of GRS 1915+105, were also found in IGR J17091–3624 with similar properties (Pahari et al. 2013a).

GRS 1915+105 is a Galactic micro-quasar which has shown spectacular X-ray variabilities since its discovery in 1992 (Castro-Tirado et al. 1994). Among different variability classes in GRS 1915+105 (Belloni et al. 2000), the ' ρ ' class shows regular, repetitive bursts in the light curve with the recurrence time between ~ 31 sec and ~ 106 sec. These recursive burst structures have been observed for extended duration and have been discussed by several authors (Taam et al. 1997; Paul et al. 1998; Yadav et al. 1999). Using the data from the Indian X-ray Astronomy Experiment (IXAE) on board the Indian Satellite *IRS-P3*, as well as *RXTE*, Yadav et al. (1999) showed that these bursts which could be categorized as irregular, quasi-regular and regular bursts have a slow exponential rise and sharp decay. Using flux-resolved spectroscopy, Pahari et al. (2013b) showed that large, repetitive oscillations in GRS 1915+105 appeared on the top of persistent emission, are consistent with the slim accretion disk approximations. Using the *Bep-poSAX* data, Massaro et al. (2010) concluded that the process, responsible for the pulses, produces strongest emission between 3.0 and 10.0 keV, and the emission at the rising phase of the pulse dominates the lower and higher energies. However, this hypothesis is not tested. Hence the consensus on the resolution of the issue with the origin of ' ρ ' class activity in GRS 1915+105 is yet to achieve. The similarity of the ρ class of GRS 1915+105 with the variability observed in IGR J17091–3624 motivates us to perform a detailed analysis of the current outburst of IGR J17091–3624.

In the present work, we consider all observations of IGR J17091–3624 between 09 February, 2011 and 15 April, 2011 with the *RXTE*/PCA and the *SWIFT*/XRT. We have analyzed both timing and spectral properties of the source after confirming that the contamination from the nearby source IGR J17098–3628 is usually very small. In section 2 we describe our analysis methods. Section 3 summarizes results regarding the hard and soft intermediate state, a fast source evolution and the transition to a ' ρ '-like class via an intermediate variability state, observed from IGR J17091–3624. Finally we compare the timing and spectral properties of the ' ρ '-like class in IGR J17091–3624 with the ' ρ ' class characteristics seen from GRS 1915+105, and discuss their implications in section 4. We give our conclusions in section 5.

2. OBSERVATIONS AND DATA ANALYSIS

We analyze all *RXTE*/PCA observations of IGR J17091–3624 between 9 February, 2011 (MJD 55601) and 15 April, 2011 (MJD 55666). Due to insufficient good time intervals and inferior quality, we are unable to extract the background data file for all High-Energy X-ray Timing Experiment (HEXTE; Rothschild et al. (1998)) observations. Hence, we use only the *RXTE*/PCA Standard-2 Science Array data and event mode GoodXenon data for our analysis. Observation details are given in Table 1. We also analyze five *RXTE*/PCA observations of GRS 1915+105 between 26 May, 1997 and 22 June, 1997 when the source was in

‘ ρ ’ class. *RXTE*/PCA consists of an array of five proportional counters (PCU0-4) filled with Xenon gas, with total effective area of $\sim 6500 \text{ cm}^2$, operating in 2.0-60.0 keV energy range (Jahoda et al. 1996). We use data observed with all Xenon layers of PCU2. During the start or the stop of any PCU unit, many observations show large count rate fluctuations in the light curve due to the instrumental effects. To take care of that, we first create xte filter file for each PCA observation and calculate good time interval (GTI) from the exposure time by applying all standard filtering criteria including breakdown events. Calculated values of good time interval are provided in Table 1. Using GTI values of individual observation, we extract background subtracted light curve from *GoodXenon* data having resolution of $125 \mu\text{s}$. Observations with the background subtracted PCA intensity $\geq 15 \text{ cts.s}^{-1}\text{PCU}^{-1}$ are considered.

We also analyze 28 archival data sets of *SWIFT*/XRT between 03 February, 2011 and 30 March, 2011. The XRT instrument on board *SWIFT* satellite has the effective area is 110 cm^2 at 1.5 keV, the position accuracy is $\sim 5 \text{ arc sec}$ and is operating in 0.2-10.0 keV energy range (Burrows et al. 2005). The typical spectral resolution of this instrument is $\sim 140 \text{ eV}$ at 6.0 keV. To avoid pile-up problem while observing luminous X-ray sources, all observations (except the first one) are performed with Windowed Timing (WT) mode which has time resolution of 2.2 ms and flux limit of $\sim 600 \text{ mCrab}$ ($\sim 200 \text{ cts/s}$) (Mineo et al. 2006). For our analysis, we use level 2 cleaned event data which has been extracted from level 1 calibrated data after applying screening criteria on specific parameters like CCD Temperature, Sun Angle, Elevation Angle etc. For all WT mode data, we assign grade 0-2 and selected good event with `STATUS==b0`. We extract source and background light curves and spectra separately using `xselect v2.4b` in `FTOOLS 6.10`.

Top panel of Fig. 1 shows the background-subtracted average *RXTE*/PCA count rate between 2.0-60.0 keV, while middle panel shows the background-subtracted average *SWIFT*/XRT count rate between 0.3-10.0 keV. HIMS & SIMS, intermediate variable state (IVS) and variable state are shown by open circles, stars and triangles respectively in the top and bottom panels of Fig. 1 while all *SWIFT*/XRT observations are shown by solid circles in the middle panel. During first 14 days of observation, IGR J17091–3624 was within the field of view of persistently luminous Z-type neutron star low mass X-ray binary GX 349+2 ($17^{\text{h}}05^{\text{m}}44.49^{\text{s}}$ (R.A. (J2000.0)), $-36^{\circ}25.38'$ (declination (J2000.0))). As a consequence, very high PCA count rate was observed in first 14 days of observation compared to the rest. Therefore, in our present work, we consider PCA observations from 23 February, 2011 onwards (observations falls right to the first vertical dotted line in the top panel of Fig. 1) to avoid the contamination effect. Further to check possible contamination from IGR J17098-3628, a transient BHXB located $9.6'$ away from IGR J17091–3624, we analyse background-subtracted image from *SWIFT*/XRT PC mode data in the energy range 0.3-10.0 keV (Fig. 2). With *SWIFT*/XRT, no X-ray source has been detected at the position of IGR J17098-3628 (shown by a circle), but is clearly detected at the position of IGR J17091–3624 (shown by a square). This is

consistent with earlier results (Krimm & Kennea 2011b). For a quantitative measurement, we calculate the count rate separately from the position of IGR J17091–3624 and from the position of IGR J17098-3628. For the energy range 0.3-10.0 keV, their values are 2.023 cts/s and 0.213 cts/s respectively on 3 February, 2011. So, at maximum, the intensity of IGR J17098-3628 is $\sim 10\%$ of IGR J17091–3624. Since, *RXTE*/PCA could not spatially resolve these sources, it is expected that at maximum $\sim 10\%$ contamination effect would be present in *RXTE*/PCA data of IGR J17091–3624.

2.1. Timing Analysis

For each PCA observation we create rms normalized and white noise subtracted power density spectrum (PDS) to study variability features and to track the spectral evolution of the source state with time. The dead time corrections are applied to the light curves. For *GoodXenon* data, the dead time per event is approximately $10 \mu\text{s}$. For details of the procedure, please check *RXTE* cookbook¹. To improve the signal-to-noise ratio in the PDS, we use the geometric re-binning of frequency bins by the factor of 1.02^2 . The expected white noise is subtracted from the PDS² and they are normalized such that their square root of integral over the range of frequencies provide fractional rms variability. We produce PDS from the *SWIFT*/XRT data using background subtracted light-curve between 0.2-10.0 keV energy range. Since one can not compare the 2.0-60.0 keV PDS from the PCA data with 0.2-10.0 keV PDS from *SWIFT*/XRT data, hence we extract only *SWIFT*/XRT PDS for observation dates when no *RXTE*/PCA data are available. Different types of QPOs and noise components are noticed in the PDS of different *RXTE*/PCA observations. The details of PDS features are given in Table 1.

2.2. Spectral Evolution

The color-color diagram (CD), the hard color vs. soft color plot and the hardness intensity diagram (HID) are created using the PCA *GoodXenon* data with 1.0 s bin time. The soft color is computed by dividing the background subtracted PCA count rates in the energy band 5.0-12.0 keV by that in the energy band 2.0-5.0 keV. Similarly, the hard color is defined as the ratio of the background subtracted count rate in the energy band 12.0-60.0 keV and 2.0-5.0 keV. X-ray intensity is defined as the background subtracted PCA count rate in 2.0–60.0 keV energy range. Since the channel gain varies from epoch to epoch, we use absolute channel ranges corresponding to each of the energy ranges to calculate soft color, hard color and X-ray intensity for the present epoch. For each *RXTE*/PCA observation, mean count rate (top panel of Fig. 1), and mean value of hard color and soft color are provided in Table 1 with errors.

2.3. Spectral Fitting

In case of *RXTE*/PCA, we perform the spectral analysis using the *Standard-2* data. While fitting, we add 1% systematic errors. In case of *SWIFT*/XRT data, we first extract an 1D image of the source. Then choosing

¹ http://heasarc.nasa.gov/docs/xte/recipes/pca_deadtime.html

² <http://heasarc.nasa.gov/xanadu/xronos/help/powspec.html>

suitable source region and background region, we extract source spectrum and background spectrum separately from the cleaned and pointed WT mode event file. We use the latest standard response matrix file (rmf) and create auxiliary response file (arf) using exposure map for the WT mode data between 0-2 grade values. We use XSpec v 12.6.0 for spectral fitting of *RXTE*/PCA and *SWIFT*/XRT data. We use 3.0–25.0 keV energy range for *RXTE*/PCA spectral analysis since the source count rate statistics is poor outside this range. We use *SWIFT*/XRT spectra in the energy range of 0.6–10.0 keV.

We have tried different single component models like `diskbb`, `compTT` or `powerlaw` as well as dual component models like `diskbb+powerlaw`, `diskbb+compTT` or `compTT+powerlaw` to fit the source spectra. The reason for selecting and testing different models is discussed in § 1. We find that the single *SWIFT*/XRT spectrum could be fitted well with a combination of `diskbb` and/or `powerlaw` model. Fitting with the rest of the model combination yields unacceptably large reduced χ^2 (> 1.5) or sometimes over-fit the spectra due to large no. of parameters. This is also true for *RXTE*/PCA spectra. Using INTEGRAL energy spectra, high energy cut-off (> 30 keV) has been detected in this source (Rodriguez et al. 2011b). A broadband BHBX spectrum, during a SIMS or HIMS, should be well described also by a combination of disk and Comptonization. Since we restrict our *RXTE*/PCA spectral analysis to 25 keV, we are unable to detect cut-off or Comptonization where electron temperature is pretty high. Thus, a relatively simple model can describe our spectra well. It may be noted that Remillard & McClintock (2006) showed that *RXTE*/PCA spectra in transient BHBXBs can be well described with a multi-temperature disk blackbody emission and a hard power-law emission with/without cut-off. While fitting *RXTE*/PCA spectra, we use a small Gaussian component at 6.4 keV in order to improve the reduced χ^2 . To account the effect of absorption by the neutral Hydrogen, all model components are multiplied by a photo-electric absorption model. The Galactic absorption column density at the direction of $17^h 11^m 12.5^s$ (R.A. (J2000.0)), $-36^\circ 24.6'$ (declination (J2000.0)) is calculated as $0.79 \times 10^{22} \text{ cm}^{-2}$. From spectral analysis, we find that for all observations, absorption column density varies between 0.82 ± 0.2 and 0.99 ± 0.3 . Thus we keep this value fixed at $0.9 \times 10^{22} \text{ cm}^{-2}$ for all spectral fitting.

3. RESULTS

SWIFT/XRT observations of IGR J17091–3624 show a transition of the source from the low count rate variability to the high count rate variability (see lower top panel of Fig. 1). Later, a gradual transition in the variability, i.e., from an irregular, less-variable state, to a regular, repetitive and large variability state has been observed. The large variability looks very similar to the unique variability observed during the ‘ ρ ’ class in GRS 1915+105 (Altamirano et al. 2011b). This motivates us to perform a detailed study on the source spectral state evolution and compare it with that of GRS 1915+105. To distinguish among variability classes, we perform the count rate fractional rms analysis of different observa-

tions (by dividing the square root of the variance with the mean count rate) from *RXTE*/PCA which is shown in the bottom panel of Fig. 1. Later, comparing with timing and spectral properties, we show that observations which have fractional rms values less than 5 are consistent with the HIMS and SIMS, and observations with fractional rms significantly higher than 5 are consistent with the variable state/ ρ -like class. A few observations show the transition between soft intermediate state and variable state/ ρ -like class, and hence described as ‘Intermediate variable state (IVS)’. The details are discussed below.

3.1. Low/hard state, hard intermediate and soft intermediate state

From 14 February, 2011 to 24 February, 2011, a gradual rise in the *SWIFT*/XRT flux between 0.3-10.0 keV is observed in IGR J17091–3624 (see middle panel of Fig. 1). Till 14 February, 2011, average *SWIFT*/XRT count rate was ~ 10 cts/s. Then it gradually increases to ~ 45 cts/s on 24 February, 2011. To check whether this rise in flux led to any state transition, we perform a detailed study on timing properties of the source using *SWIFT*/XRT data. From 09 February, 2011 to 18 February, 2011 the PDS usually show band-limited noise, sometimes with the rms amplitude as strong as $\sim 9\%$ (see Table 1) and can be decomposed into multiple broad Lorentzians. Apart from this, a break in the PDS is observed once at ~ 0.19 Hz. Broad but strong QPO-like features are observed at least twice at ~ 0.2 Hz (with Q-factor > 2 ; see Table 1). All these features in the PDS can easily be associated with the low/hard state (LS) (Belloni et al. 2005). On 20 February, 2011, a type-C QPO at ~ 0.51 Hz along with the strong flat-top noise ($\sim 7\%$ rms) is observed in the PDS, which carries the signature of the hard intermediate state (HIMS). This imply that the source undergoes state transition from the LS to the HIMS. On 22 February, 2011, a broad Lorentzian (quality factor < 2) is observed at ~ 1.8 Hz along with weak red noise (~ 2 -3% rms) in the *SWIFT*/XRT spectra which may indicate that the source undergoes another transition from the HIMS to the soft intermediate state (SIMS). Detection of the type-B QPO on 23 February, 2011 using *RXTE*/PCA (see Table 1) confirms the transition (Belloni et al. 2005). Rodriguez et al. (2011b) also observed the LS/HIMS to SIMS transition based on the detection of optically thin radio emission on MJD 55623.57 (03 March, 2011). From 24 February, 2011 to 13 March, 2011, the source usually shows back and forth transition between the HIMS and the SIMS with the usual detection of type-C and type-B QPOs respectively (see Table 1). In Fig. 3, we have shown example of the HIMS observed on 26 February, 2011 and the SIMS observed on 03 March, 2011. Top panels show the PDS where the HIMS shows strong flat-top noise ($\sim 8\%$ rms amplitude) with a strong type-C QPO at 3.73 ± 0.09 Hz but the SIMS show weak red noise ($\sim 3\%$ rms amplitude) with a transient type-B QPO at 4.85 ± 0.08 Hz. For more accurate determination of the state, we perform time-lag analysis between the the soft energy band (1.8–4.2 keV) and the hard energy band (5.0–13.0 keV) using GHATS v1.0.2 (T. Belloni, private communications) where the lag formulation is based on cross-spectra technique. At the fundamental QPO frequency, HIMS shows the soft-

lag (soft photons lag hard photons) of ~ 8 msec (middle left panel of Fig. 3) while the SIMS at the fundamental QPO frequency shows hard-lag of ~ 22 msec (middle right panel of Fig. 3). In both panels, lags at the fundamental QPO frequency are shown by dotted vertical lines. These observations are in fine tune with the characteristics of these states.

We also carry out energy spectral analysis of observations between 09 February, 2011 and 25 March, 2011 respectively. From the fitted parameters in Table 2, we find that disk component is not significant while fitting the spectra observed between 09 February, 2011 and 20 February, 2011. A single power-law can adequately describe these spectra. From 20 February, 2011 onwards a soft disk component is essentially present in all spectral fitting and the power-law becomes steeper (see Table 2). This indicate that a hard-to-soft state transition takes place. This is consistent with the PDS characteristics where the transition from the LS/HIMS to the SIMS is observed. An example of *RXTE*/PCA spectral fitting of the HIMS and the SIMS are shown in the bottom left and bottom right panel of Fig.3 respectively. From Table 2, it is clear that all low flux state observations (till 19 February, 2011) have photon index value less than 1.8 and no disk component is present at the detectable limit of *SWIFT*/XRT. These along with the detection of band-limited noise meet the criteria of a low/hard state as observed in transient BHXBs (Homan & Belloni 2005; Remillard & McClintock 2006; Belloni et al. 2005). However, a single power-law still provides a good fit (an F-test between `powerlaw` and `diskbb+powerlaw` models yields a probability of 1.7×10^{-10}) of the energy spectra on 20 February, 2011, where the LS to the HIMS transition is observed. Insignificant disk contribution during this transition is may be either due to very low disk flux of the source or very low temperature of the disk (< 0.6 keV). Disk flux contribution is ~ 10 -20% of the total flux in other HIMS where disk is detected significantly (see Table 2).

It may be noted that the X-ray spectral state transition is observed between 18-22 February, 2011 is based only on *SWIFT*/XRT data in the energy range 0.2-10.0 keV since there are no simultaneous observation of *RXTE*/PCA between 9-22 February, 2011. Hence the robustness of the result, based on XRT PDS, cannot be established confidently although it is consistent with the detection of radio flares on MJD 55601.3 and 55605.6 (Rodriguez et al. 2011b) and show correct trend in spectral evolution, usually observed from normal transients (Homan & Belloni 2005; Belloni et al. 2005). Due to this ambiguity, we put question marks in first five observations of state classification column in Table 1, where PDS features are not clear. However, our spectral analysis agrees well with spectral parameters obtained from the joint spectral analysis of *INTEGRAL*/IBIS and *SWIFT*/XRT data by Capitanio et al. (2012). The relatively small difference between both results may be due to the (1) use of cut-off power-law (where cut-off energy > 70 keV, see Table 1 of Capitanio et al. (2012)) (2) different absorption column density (1.1 ± 0.3).

The outburst evolution of the source through the LS, HIMS & SIMS and frequent to and fro transition between the HIMS and the SIMS (see Table 1) indicate that the disk is unstable and the evolution pattern roughly fol-

lows the outburst evolution observed in normal transient BHXBs (Homan & Belloni 2005; Belloni et al. 2005).

3.2. Intermediate variable state

During the continuous monitoring of the PCA light curve in IGR J17091–3624, we find a gradual transition in the count rate variability pattern from 12 March, 2011 to 19 March, 2011 in the energy range 2.0-60.0 keV. On 12 March, 2011, the source was in the SIMS when the light curve is less variable and very similar to the typical light curves seen in canonical BHXBs (see the top left panel of Fig. 4). On 19 March, 2011, the light curve shows a very regular repetitive pattern, high variability (peak count rate ~ 3 –4 times higher than the count rate at the persistent level; see lower-middle left panel of Fig. 4), and high count rate fractional rms (see bottom panel of Fig.1). We denote it by variable state/ ρ -like class. Observations of average count rate that belong to the HIMS/SIMS and variable state/ ρ -like class are separated by a dashed vertical line in Fig. 1.

The transition between the SIMS and the variable state occurs through some semi-oscillatory intermediate stage on 14 March, 2011. The random noisy pattern which is observed during the SIMS on 12 March, 2011, appears to be superimposed on an X-ray intensity oscillation with the timescale of ~ 80 –100 sec in the light curve on 14 March, 2011 (upper-middle left panel of Fig.4). The superimposed pulsations on random fluctuations are called intermediate variable state (IVS). Although these intermediate phases are transient but it has been observed few times like on 18, 23, 24 & 26 March, 2011, when the source oscillates between the SIMS like random fluctuations and the highly variable ρ -like pulsations (see Table 1). The rms normalized PDS during the IVS show characteristic oscillations in the frequency range of ~ 11 –14 mHz with a variable quality factor between 3–9. They are usually associated with very weak red noise having rms amplitude 2-4% and weak, narrow QPOs (see Table 1 and upper-middle right panel of Fig. 4). The IVS on 24 March, 2011 shows broad Lorentzian noise along with a type-A QPO at ~ 8 Hz. Recently, a 11 mHz oscillation is discovered in the PDS using *Chandra* data during the HIMS in the BHXB H1743-322 (Altamirano & Strohmayer 2012a). However, the origin of 11 mHz oscillations in both sources may be different. From the middle right panels of Fig. 4, it is clear that IVS is distinctively different from the variable state/ ρ -like class because (1) mHz pulsations in the IVS never show harmonics which, on the other hand, is frequently observed in variable state (lower middle right panel of Fig. 4). The absence of harmonics in the IVS may be due to very low count rate statistics associated with the PDS. (2) The characteristic oscillation frequency of the variable state is always higher than that of IVS and (3) rms amplitude of the continuum in variable state (~ 10 -15%) is significantly higher than that of the IVS (~ 5 –7%). The term ‘intermediate’ is used as it is observed between the SIMS, where no mHz QPOs are observed (top right panel of Fig. 4), and the ρ -like class where very strong mHz oscillations are noticed. Thus, IVS can be treated as the beginning of the ρ -like class in IGR J17091–3624. To trace any change in spectral state during this transition, we plot the HID (bottom left panel of Fig. 4) and the CD (bottom right panel of Fig. 4).

From the CD and the HID it may be noted that both IVS and SIMS nearly coincide with each other (shown in red and black) while the variable state shows a softer and brighter part (shown in blue) which is absent in both SIMS and IVS. Hence, IVS has similar characteristics of SIMS with large amplitude oscillations superimposed to random fluctuations. The energy spectral analysis of the IVS between 3.0–25.0 keV on 14 March, 2011 shows that the spectrum can be well fitted by the `diskbb+powerlaw` model which shows parameters similar to the SIMS. Using numerical solutions, Janiuk & Misra (2012) noticed that the limit cycle oscillations are observed when the viscosity fluctuation amplitude are small in an unstable disk. The pulsating behavior disappears and random fluctuations are restored when stochastic fluctuation amplitude exceeds a critical limit. However, random fluctuations and mHz oscillations can also co-exist. This model can explain results qualitatively from Fig. 4.

3.3. Variable state/ ρ -like class

The new variable state/ ρ -like class remains stable for almost 25 days (19 March, 2011 – 12 April, 2011; see Table 1) except 23, 24, 25 & 26 March, 2011. The recurrent time scale of this variability is found to change with time. Fig. 5 shows the evolution of the source via five *RXTE*/PCA light curves from 19 March, 2011 to 10 April, 2011. On 19 March, 2011, the variability timescale of recursive bursts is ~ 33.8 sec and the ratio of peak count rate to the persistent level count rate is 2.92 ± 0.05 . These bursts have simple profiles with slow-rise and fast-decay. Light curves in Fig. 5 show that, as these bursts evolve with time, flaring frequency roughly increases. On 10 April, 2011, the recurrence time scale of the variability becomes ~ 21.7 sec. and the burst becomes more structured. The ratio of peak count rate to the persistent level count rate becomes 3.38 ± 0.06 . Careful observation of burst profiles in Fig. 5 reveals two unique burst structures (1) Burst profile seen on 31 March, 2011 have a single peak and the count rate rises slowly (~ 30 sec) to the peak of the burst. (2) Burst profile seen on 03 April, 2011 can be characterized by double peak and show faster rise in count rate (~ 15 -20 sec). This behavior and the variation in burst profile structures of the source has so far been seen in the ' ρ ' class of GRS 1915+105. From Table 1, it is clear that ρ -like variabilities in IGR J17091–3624 becomes stronger (i.e., rms amplitude of characteristic oscillations increases from $\sim 6\%$ to $\sim 32\%$) and faster (i.e., recurrence timescale decreases from ~ 80 sec (on 24 March, 2011) to ~ 22 sec (12 April, 2011)) with time.

For each variable state observation, we fit the PDS continuum with the broken power-law model (since low frequency break is prominent; see top panel of Fig. 6) and we use Lorentzian to fit characteristic pulsation peaks and broad noise components. From Table 1, PDS fit shows that most of the time, the characteristic pulsation frequency appears along with the first harmonic (e.g., ~ 30 and 62 mHz on 19 March, ~ 24 and 50 mHz on 29 March etc.), a few times with both first and second harmonics (e.g., ~ 31 , 63 and 110.4 mHz on 20 March, ~ 34 , 68 and 110.2 mHz on 02 April etc.). We also detect type-A QPOs around 7–9 Hz during this state. An example of fitted PDS during variable state on 31 March, 2011 is shown on the top left panel of Fig. 6. In the bottom left panel of Fig. 6, we show the time evolution

of characteristic oscillation frequencies of ρ class in both IGR J17091–3624 and GRS 1915+105. This panel indicates that IGR J17091–3624 shows faster time evolution of characteristic pulsation frequency than that of GRS 1915+105 by a factor of ~ 1.3 (measured by the change in characteristic oscillation frequencies in the given period provided in the bottom left panel of Fig. 6). In order to check how these recurrent bursts lose their quality factors with time, we plot the q-factor and fractional rms amplitude (%) of the variable state characteristic oscillations with time in the top right panel of Fig. 6. It shows a random fluctuation in the q-factor, which is, unrelated with the fractional rms amplitude as well as the pulsation period. A closer inspection show that from day 20 onwards, the quality factor of characteristic pulsations overall drops by a factor of ~ 6 , while during the same time, fractional rms amplitude roughly increases. Thus, highly coherent characteristic pulsations in the variable state/ ρ -like class seem to be changed into the broad Lorentzian component at the end of their evolution. This is also reflected from the PDS fit on 15 April, 2011 (see Table 1) when multiple broad Lorentzian components appear during the transition from the ρ -like class to some other variability classes (may be similar to the κ/λ class in GRS 1915+105). A correlation is observed between the pulsation frequency of characteristic oscillations and its fractional rms amplitude (%) (shown in bottom right panel of Fig. 6) with the Pearson product moment correlation coefficient (PMCC) of 0.91 (Sheskin 2003).

In the following section, we explore other properties of the variable state/ ρ -like class and compare them with those of GRS 1915+105.

3.3.1. Properties of variable state/ ρ -like class in comparison to GRS 1915+105

As the variable state/ ρ -like class in IGR J17091–3624 looks similar to the ' ρ ' class of GRS 1915+105, we make a comparative study between them.

All panels of Fig. 7 show the 2.0-60.0 keV light curve in both sources. To track the change in variability pattern, we consider two observations of variable state/ ρ -like class in IGR J17091–3624 which show transition from the slow variability & low peak flux (31 March, 11; top left panel of Fig. 7) to the fast variability & high peak flux (10 April, 11; bottom left panel of Fig. 7). Similar transition from the slow variability & low peak flux on 26 May, 1997 (top right panel of Fig. 6) to the fast variability & high peak flux on 22 June, 1997 (bottom right panel of Fig. 7) is also observed in GRS 1915+105. However, it is interesting to observe that the average peak count of bursts in GRS 1915+105 increases significantly while transiting from the slow variability to the fast variability (~ 4000 cts/s/PCU to ~ 5000 cts/s/PCU) while it is increased slightly (~ 400 cts/s/PCU to ~ 430 cts/s/PCU) in IGR J17091–3624 during the variable state/ ρ -like class. It may be noted that the variability in IGR J17091–3624, although repetitive, is irregular, less structured (as the source is fainter than GRS 1915+105) and less coherent (i.e., q-factor is lowered by a factor of 1.4–1.8) compared to the ' ρ ' class of GRS 1915+105. In both sources, double-peak bursts are more frequent during fast variability regime.

Previously, a strong anti-correlation between the X-

ray intensity and the hardness ratio (defined as the ratio of count rate between 12.0–60.0 keV and 2.0–12.0 keV) is found in the ‘ ρ ’ class of GRS 1915+105 (Yadav et al. 1999). This anti-correlation is also found in the variable state/ ρ -like class of IGR J17091–3624. Fig. 8 shows the comparative result on the anti-correlation found in IGR J17091–3624 on 31 March, 2011 (top and bottom left panels) and in GRS 1915+105 on 22 June, 1997 (top and bottom right panels). It is clear that at every second on burst profile, the hardness ratio is higher in IGR J17091–3624 than that observed in GRS 1915+105.

To study the nature of bursts in details, we study the rise and decay profiles from both sources. Top left panel of Fig. 9 shows the combined rise profiles of several bursts and combined decay profiles of same bursts in IGR J17091–3624 on 31 March 11. To study the average behaviour of rise profiles, we normalize the starting time of each profile to 0 sec. Similarly, to study the average behavior of decay profiles, we normalize the starting time of the decay of each profile to 15 sec. We repeat the same procedure for the ρ class observation in GRS 1915+105 on 22 June, 1997 (shown in the top right panel of Fig. 9) except for the fact that the starting time of each decay profile is normalized to 70 sec. We fit the combined rise profile with exponential rise function $f_{rise}(t) = ae^{t/t_{rise}}$ (red continuous line), the combined decay profile with exponential decay function $f_{decay}(t) = ae^{-t/t_{fall}}$ (blue continuous line) and all profiles with straight line (red and blue dotted line). In case of GRS 1915+105, exponential function fits better than straight line in both rise and decay profile with the significance of $> 10\sigma$ and $> 8\sigma$ respectively, where the significance is estimated using F-test. For IGR J17091–3624, the corresponding significance values are 3.2σ and 5.1σ respectively. The slope of the exponential function, for both rise and decay, are found similar in both sources (see Table 3). If burst structures depend on physical processes associated with the origin of the bursts (Nielsen et al. 2012), then our results indicate that the origin of burst structure may be similar in both sources. We also study energy-dependent light curve variance spectra in both sources during their ‘heartbeat’ oscillations. The variance spectrum in IGR J17091–3624 on 31 March, 2011 (bottom left panel of Fig. 9) shows that lightcurve variance decreases monotonously with energy. However, the variance spectrum in GRS 1915+105 on 22 June, 1997 (bottom right panel of Fig. 9) shows an initial increase in variance with the energy till ~ 6 keV, then it decreases significantly, at least, up to ~ 14 keV. This is remarkable as it may indicate that although similar parameter may trigger bursts in both sources, the spectroscopic evolution of the bursts is different, which, however, need to explore further.

Top panels of Fig. 10 show that the low frequency (0.1–10.0 Hz) continuum power, characteristic pulsation & its harmonics and the nature of low frequency noise components are similar during ρ class in both sources. White noise subtraction is not applied only for PDS shown in the top panels of Fig. 10. High frequency power in noise continuum becomes very weak above 1 Hz in case of IGR J17091–3624 (top left panel of Fig. 10 and top right panel of Fig. 4) although type-A/type-B QPOs are observed few times in the PDS. On the other hand, the

strong, powerlaw like noise continuum in GRS 1915+105 continues at higher frequencies (at least up to 10 Hz; top right panel of Fig. 10) along with a type-B QPO at 6.7 ± 0.4 Hz (middle right panel of Fig. 10). Interestingly, the 6.7 ± 0.4 Hz type-B QPO in GRS 1915+105 also has the harmonic at 13.2 ± 0.8 Hz with the quality-factor of 3.8 ± 0.4 (middle right panel of Fig. 10). Along with characteristic heartbeat oscillations, IGR J17091–3624 show 7–10 Hz type-A QPOs on 24, 25, 31 March, 2011 and 03 April, 2011 (see Table 1) and type-B QPO once at ~ 5 Hz on 12 April, 2011 (see Table 1). May be because of statistical limit, harmonics in type-A/type-B QPOs are not visible in IGR J17091–3624. An example of type-A QPO observed during the ρ -like class on 31 March, 2011 at ~ 8.4 Hz, is shown in the middle left panel of Fig. 10. Harmonics at mHz frequency are seen in both sources. Lower panels of Fig. 10 show the comparative study of the HIDs between two sources. We find similar trend in the HID evolution but different range in hard color for both sources. Results on comparative study of both sources are summarized in Table 3.

During 2011 outburst, IGR J17091–3624 evolves from the LS/HIMS to the SIMS state and finally from the SIMS to the variable state/ ρ -like class (similar to ρ class in GRS 1915+105) as X-ray flux increases (see Table 1 of Capitanio et al. (2012) and Table 1 & 2 from our analysis). Detection of accretion disk wind as well as quenching of radio emission during disk dominated state may suggest that IGR J17091–3624 is approaching the high soft state (King et al. 2012; Rodriguez et al. 2011b).

According to the X-ray observations, IGR J17091–3624 passes through the SIMS state during radio flares observed on MJD 55623.57 (Rodriguez et al. 2011b). Generally, HIMS to SIMS transitions are followed by Radio flares (Belloni et al. 2005). Following the SIMS, large amplitude X-ray oscillations appear via the intermediate variable state and continues for ~ 25 days (MJD 55638 – MJD 55663). Similarly, GRS 1915+105 was in the HIMS state during 26 March, 1997 – 8 May, 1997 (Rao et al. 2000) and the ρ X-ray class activity started on 26 May, 1997 and continue till 25 June, 1997 (Yadav et al. 1999). Between these periods (i.e., 8–26 May, 1997), for a short time, GRS 1915+105 showed Radio flare on 15 May, 1997 (Mirabel et al. 1998). We analyse and fit the *RXTE*/PCA PDS on 13 May, 1997 using the combination of broken powerlaw and Lorentzian and find a type-B QPO at 5.87 ± 0.12 Hz, with the quality factor of 7.89 ± 0.62 and fractional rms amplitude (%) of 4.84 ± 0.36 . The PDS is associated with weak red noise. These two observations show that the source was in the SIMS state on 13 May, 1997. Thus, GRS 1915+105 also passes through the SIMS before its large amplitude oscillations begin. This indicates that the X-ray spectral evolution prior to the ρ class activity in both sources are roughly similar. This also strengthen that the spectroscopic nature of the origin of ρ class activities in both sources may be similar.

4. DISCUSSION

In this paper, we study the evolution of the X-ray activity in IGR J17091–3624 from 3 February, 2011 to 15 April, 2011. Initially, with the increase in the *SWIFT*/XRT count rate, transition from the low/hard and hard intermediate state to the soft inter-

mediate state has been detected. In transient BHBs, this transition is usually accompanied by Radio flares (Fender, Belloni & Gallo 2004; Belloni et al. 2005). Our results show that the source makes to and fro transition between the HIMS and the SIMS a few times. This may represent the disk instability which occurs due to the increasing mass accretion rate. A few days later, a transition takes place from the SIMS to a regular, repetitive and highly variable pulsations similar to the ρ -class variability, previously observed only from GRS 1915+105. A few observations between variable state/ ρ -like class and the SIMS show ~ 11 -14 mHz quasi-periodic variabilities with low rms amplitude which we term as intermediate variable state.

In addition to the structural similarities of ‘heartbeat’ oscillations in both sources, we find that they show similar time evolution in the burst structure. With time, characteristic pulsation frequency increases in both sources as well as the ratio of the peak flux to the persistent level flux also increases. In both cases, average rise profile of the burst shows slow exponential rise while average decay profile shows fast decay. Interestingly, we find strong anti-correlation between hardness value and the X-ray flux during variabilities in both sources. The evolution of the burst structure in the HID of both sources is identical. PDS below 1 Hz, show similar noise continuity as well pulsation peaks. Both sources have strong mHz QPOs along with harmonics and strong flat-top noise along with the presence of type-A/type-B QPOs in the PDS.

In other BHBs, transition from the canonical low/hard state to the steep power law (SPL) state (highest flux regime of the outburst) (Remillard & McClintock 2006), which sometimes coincides with the soft intermediate state (Fender, Belloni & Gallo 2004; Belloni et al. 2005), is a commonly observed phenomenon. IGR J17091–3624 also shows transition from the LS/HIMS to the SIMS and the high soft state. Spectral properties of the low/hard state, HIMS and SIMS in IGR J17091–3624 also match with those of other BHBs (Remillard & McClintock 2006; Belloni et al. 2005). Lutovinov et al. (2003) showed evidences that previously IGR J17091–3624 was in the low/hard state. A recent report (Altamirano et al. 2013) claims that IGR J17091–3624 is going back to quiescence similar to normal transient BHBs. It is important to note that GRS 1915+105 was discovered as a normal transient in 1992 (Lochner et al. 1992). It was detected at the intensity level as low as ~ 90 mCrab and gradually increased up to 300 mCrab over a month period (Greiner 1994). Hence it is possible that at the beginning, similar to IGR J17091–3624 and normal transients, GRS 1915+105 also evolved from quiescence and passing through the low/hard, HIMS and SIMS, it entered into different variability classes. Following the fate of IGR J17091–3624 and other normal transients, GRS 1915+105 may also fade into quiescence in the future. Therefore, it is possible that at the beginning, the spectral evolution of GRS 1915+105 and IGR J17091–3624 are similar to normal transients. With the *RXTE*/PCA, GRS 1915+105 has usually been seen in the HIMS/SIMS state, but never seen in the typical low hard state. From the HIMS and SIMS state, IGR J17091–3624 deviates from the canonical BHB

track and shows regular repetitive variabilities similar to the ρ class variability observed in GRS 1915+105. Besides, within *RXTE* era, IGR J17091–3624 shows six variability classes (Altamirano et al. 2011c) out of 14 classes in GRS 1915+105 (Belloni et al. 2000; Klein-Wolt et al. 2002). Thus considering evidences, IGR J17091–3624 do show spectral evolution and properties similar to GRS 1915+105, but, during first ~ 40 days of the outburst, it also clearly exhibits outburst evolution properties similar to other canonical BHBs (more evidently than GRS 1915+105).

Our results tentatively indicate that the central object in IGR J17091–3624 system may be a black hole. One such indication is the detection of type-B QPOs from six different observations and type-C QPOs from eight different observations (see Table 1). These QPOs are often observed from BHBs rather than from NSXBs (Casella et al. 2005; Belloni et al. 2005). Besides, the observation of low frequency break in the PDS of this source on 15 February, 2011 (also see, Lutovinov et al. (2003)) further decreases the chance of being NSXB. Moreover, from our analysis, type-I X-ray bursts are not found in any observations within about two months. These bursts are unique characteristics of neutron star LMXBs (Fujimoto et al. 1981; Lewin et al. 1995; Bhattacharyya 2010). This gives an indirect evidence that the source may not be a neutron star.

We find few dissimilarities between the variable state/ ρ -like class of IGR J17091–3624 and the ‘ ρ ’ class of GRS 1915+105. They are listed below:

1. The color-color diagram (CD) of the ‘ ρ ’ class shows a loop-like pattern (see Belloni et al. (2000)) while the CD of the variable state/ ρ -like class in IGR J17091–3624 shows a patchy pattern (see bottom right panel of Fig. 4). Low count rate and irregular burst structure may cause such randomness in the CD. In the HID, GRS 1915+105 traverses a clockwise loop while the IGR J17091–3624 traverses anti-clockwise (Altamirano & Belloni 2012b). The X-ray flux from IGR J17091–3624 is significantly lower than that observed from GRS 1915+105 even considering a distance as large as ~ 17 kpc.
2. An interesting difference between two systems is that the hardness ratio during ρ class activity is higher (~ 2 times) in IGR J17091–3624 than that observed in GRS 1915+105. One possible reason for this higher hardness value, as discussed in Altamirano et al. (2011c), is the distance of IGR J17091–3624 is higher compared to the distance of GRS 1915+105. However, using *SWIFT*/XRT data, we find that the absorption column density is 0.9 – 1.02×10^{22} cm $^{-2}$ for IGR J17091–3624 while this value is 5 – 13.6×10^{22} cm $^{-2}$ for GRS 1915+105. Hence along with large distance, effects like the presence of the strong disk wind or large disk inclination angle (King et al. 2012) may also cause the observed flux difference between two sources. The contamination from a nearby source is not favored since the hardening of the lightcurve during the heartbeat oscillations has also been observed with the *SWIFT*/XRT (Capitanio et al. 2012).

3. Typical low/hard state observations where disk emission is not visible, are commonly seen in canonical BHBs but have never been seen in GRS 1915+105 during the RXTE era. Earlier outbursts in IGR J17091–3624 were started with the LS (Lutovinov et al. 2003; Capitanio et al. 2006). In case of 2011 outburst, *SWIFT*/XRT spectral fitting of IGR J17091–3624 shows that, from 9 February, 2011 to 20 February, 2011 (see Table 2) disk component is not visible in the spectra. Apart from this, a break in the PDS continuum, detection of broad Lorentzian also indicate that the present outburst started with the LS although accurate determination of spectral state is not possible due to unavailability of *RXTE* data.

4. A systematic study of the occurrence of different classes in GRS 1915+105 (Yadav & Pahari 2013) show that the ρ class variability eventually arise from the α or ω class after transiting from the SIMS. These are different X-ray classes with large variation in the variability timescale as well as X-ray flux (Belloni et al. 2000; Klein-Wolt et al. 2002; Pahari & Pal 2010). Until now, the ρ class like activity in IGR J17091–3624 arises from the SIMS through the IVS, skipping any other variabilities as observed in GRS 1915+105.

5. From Table 1, the total good time interval of variable state/ ρ -like class observations in IGR J17091–3624 can be estimated as ~ 19.87 hours. Once in the entire ρ class period (19 March, 2011 to 12 April, 2011), it goes back to the non-variable SIMS (25 March, 2011). During the rise phase of 1997 outburst in GRS 1915+105 also was in the SIMS prior to ρ class on 26 May, 1997 and showed a transition from the ρ class to the κ class on 18 June, 1997 (Yadav & Pahari 2013). In GRS 1915+105, the total good time interval of ρ class observations is found to be ~ 7.36 hours. Unlike IGR J17091–3624, GRS 1915+105 occasionally make transition to α or κ class within ρ class period (Yadav & Pahari 2013). These observations, in both sources, indicate that ‘ ρ ’ class variability may represent very stable X-ray class. If frequent observations and the total good time interval are assumed to represent the stability of a state, then the possible reason for prolonged stability of IGR J17091–3624 in the variable state/ ρ -like class compared to GRS 1915+105 may be the lower mass accretion rate in IGR J17091–3624 compared to GRS 1915+105 which, however, needed to be explored further.

Using the radio data, Rodriguez et al. (2011b) found the distance of IGR J17091–3624 to be 10–17 kpc assuming black hole mass to be $10 M_{\odot}$. Later, Rebusco et al. (2012) estimated the mass of $6 M_{\odot}$. We assume here the black hole mass to be $8 \pm 2 M_{\odot}$. We use the distance of IGR J17091–3624 to be 14 ± 3 kpc to calculate the mass accretion rate of IGR J17091–3624 relative to the GRS 1915+105. In case of GRS 1915+105, we assume the mass, the distance and the disk inclination angle with respect to observer’s line of sight to be

$10.1 \pm 0.4 M_{\odot}$ (Steehgs et al. 2013), 12.5 ± 2.1 kpc and 70° (Muno et al. 1999) respectively. The mass accretion rate at the inner disk can be derived using the energy conservation law and the Virial theorem. Using simple analytical approach and assuming the disk radiation to be blackbody & considering both side of the disk, the mass accretion rate is (Frank, King & Raine 2002) :

$$\dot{m} = 8\pi R_{in,km}^3 \sigma T_{in,keV}^4 / 3GM_{bh} M_{\odot} yr^{-1} \quad (1)$$

where σ is the Boltzmann constant, G is the gravitational constant and $T_{in,keV}$ is the inner disk temperature in keV and $R_{in,km}$ is given by the equation

$$R_{in,km} = C^2 \times \sqrt{N_{diskbb}} \times D_{10,kpc} / \sqrt{\cos i} \quad (2)$$

where C is the color correction factor (assumed to be ~ 1.8 in case of black hole (Kubota et al. 1998)), N_{diskbb} is the normalization corresponds to the *diskbb* model component in *XSpec*, $D_{10,kpc}$ is the distance to the source in the unit of 10 kpc and i is the disk inclination angle with respect to observer’s line of sight. Inserting the equation (2) in (1), we get

$$\dot{m} = \frac{8\pi\sigma T_{in,keV}^4}{3GM_{bh}} \times (C^2 \times \sqrt{N_{diskbb}} \times D_{10,kpc} / \sqrt{\cos i})^3 \quad (3)$$

To obtain a qualitative idea, we compare accretion parameters of both sources using above equations. For example, the spectral analysis of a less-variable, HIMS observation in GRS 1915+105 on 09 September, 1997 using *RXTE*/PCA yields the disk temperature of 1.24 ± 0.03 keV and inner disk radius of 57 ± 3 km (Muno et al. 1999). Using equation (2), the equivalent normalization would be 211.3 ± 26.5 . From the spectral analysis of non-variable, HIMS in IGR J17091–3624, observed on 08 March, 2011, we find the value of N_{diskbb} to be 13.87 ± 1.35 and the disk temperature to be 1.24 ± 0.03 keV (See Table 2). Using these values in equation (3) and assuming disk inclination angle (i) to be 70° in IGR J17091–3624 (King et al. 2012; Capitanio et al. 2012), we find $\dot{m}_{GRS1915+105} / \dot{m}_{IGRJ17091-3624} \sim 48.3 \pm 8.7$. Hence, the mass accretion rate in GRS 1915+105 is significantly higher (may be in the order of magnitude) compared to that of IGR J17091–3624. This may be consistent with very high X-ray flux observed in GRS 1915+105 than that seen from IGR J17091–3624 even considering IGR J17091–3624 at larger distance. We also calculate the relative viscous timescale of the accretion flow using the following relation (Frank, King & Raine 2002):

$$t_{vis}^d = 4.3 \times 10^{-4} \alpha^{-1} \dot{m}_d^{-1} M_{bh}^{-1} R_{in,km}^2 s \quad (4)$$

where t_{vis}^d is the dynamic viscous timescale, α is the viscosity parameter. We consider the typical value of α to be 0.01 for both sources. Using relation (4) and above parameters, we find the value of $t_{vis|GRS1915+105}^d / t_{vis|IGRJ17091-3624}^d$ to be $\approx 0.37 \pm 0.13$ when the disk inclination angle of IGR J17091–3624 is $\sim 70^{\circ}$ (King et al. 2012; Capitanio et al. 2012). Hence the viscous timescale of GRS 1915+105 is smaller relative to IGR J17091–3624 in non-variable state.

5. CONCLUSIONS

From our analysis of *SWIFT*/XRT and *RXTE*/PCA data during 2011 outburst of IGR J17091–3624, and using results from comparative study of timing and spectral properties with GRS 1915+105, we conclude following points.

1. We find that IGR J17091–3624 is the only known transient LMXB, which shows regular, repetitive and structured variability in the intensity pattern similar to the ρ -type variability seen from GRS 1915+105. Various parameters like burst frequency evolution, burst structure profile, rise and decay profile, peak-to-minimum flux ratio, harmonics of mHz characteristic pulsations and PDS characteristics show remarkable similarity. The entry to the ρ -type variability in IGR J17091–3624 is from the SIMS via intermediate variability state which show ~ 11 -14 mHz coherent pulsations with the presence of weak red noise/type-A QPO, while the exit from the ρ -type variability is through the soft state with several broad Lorentzian noise components and QPO-like feature at ~ 3 Hz (similar to the κ/λ class; see Table 1). GRS 1915+105 also was in the SIMS prior to ρ class on 26 May, 1997 and showed a transition from the ρ class to the κ class on 18 June, 1997 (Yadav & Pahari 2013). However, significant differences in hardness ratio as well as variance spectra are also observed.
2. Several evidences like power-law dominated spectra, the detection of type-B and type-C QPOs, break in PDS continuum along with ρ class activity (as seen in GRS 1915+105 which is a BHXB) are consistent with the black hole identification of the source.
3. The source shows increase in flux while transiting from the low/hard state/HIMS to the SIMS. Later a transition occurs from a typical irregular variability state (SIMS), seen commonly in most of the BHXBs to the regular, repetitive large variability state, seen only in GRS 1915+105 (ρ' -type variability) via an intermediate state. However, X-ray bursts during variability state/ ρ -like class are spectrally harder than that found in GRS 1915+105. Central black hole mass, its distance, disk inclination angle, absorption column density etc. may be important to explain the observed hardness ratio but at present we do not know exact answer. It is a topic for future investigations if these parameters or some unknown parameter/mechanism is responsible for higher hardness ratio during ρ class activity in IGR J17091–3624.
4. From Table 1, it is clear that we detect several QPOs ranging from few mHz to 10 Hz or so. Not only that, there are to and fro transition between the HIMS and the SIMS and the source show evolution of characteristic oscillations in ρ -class faster than GRS 1915+105.
5. In both sources, ' ρ ' class activity is observed following the soft intermediate state where disk emission in the energy spectra is visible and contribute

significantly to the total flux. GRS 1915+105 during the *RXTE* era, never shows typical low/hard state where disk emission is not visible but IGR J17091–3624 shows low hard state where disk emission is not significant. This result agrees well with the low hard state observations of other black hole X-ray binaries. Similar to a normal transient, IGR J17091–3624 also seems to move to the quiescence as observed with *SWIFT*/XRT (Altamirano et al. 2013). Hence considering evidences, IGR J17091–3624, behaves similar to GRS 1915+105 at certain period of evolution whereas it behaves like other canonical BHXBs at some other period of evolution. Hence, this source may be an important bridge between GRS 1915+105 and other canonical BHXBs in understanding observational dissimilarities, as well as accretion and radiation mechanisms.

Thus long term and continuous observation of outbursts of this source in multi-wavelength band using *ASTROSAT* would reveal a lot of information regarding the radiation mechanism and accretion flow properties of BHXBs, and help to construct the complete picture of accretion flow around black hole systems by connecting GRS 1915+105 with other canonical BHXB systems.

6. ACKNOWLEDGEMENTS

We thank the referee for his/her constructive comments which helps to improve the work. We also thank another referee Ron Remillard for useful discussions. MP is thankful to Ranjeev Misra for constructive discussions. We thank T. Belloni for providing GHATS v1.0.2 timing analysis software. This research has made use of the General High-energy Aperiodic Timing Software (GHATS) package developed by T.M. Belloni at INAF - Osservatorio Astronomico di Brera and data obtained through the High Energy Astrophysics Science Archive Research Center online service, provided by the NASA/Goddard Space Flight Center and the *SWIFT* data center.

1154 Altamirano, D., Wijnands, R., & Belloni, T., 2013, *Astron.*
1155 *Telegram*, 5112, 1

1156 Altamirano, D., Strohmayer, T., 2012a, *ApJ*, 754, L23

1157 Altamirano, D. & Belloni, T. 2012b, *ApJ*, 747, L4

1158 Altamirano, D., Linares, M., van der Klis, M., Wijnands, R.,
1159 Kalamkar, M., Casella, P., Watts, A. & Patruno, A. 2011a,
1160 *Astron. Telegram*, 3225, 1

1161 Altamirano, D., Belloni, T., Krimm, H. A., Casella, P., Curran,
1162 P., Kennea, J. A., Kalamkar, M. & van der Klis, M. 2011b,
1163 *Astron. Telegram*, 3230, 1

1164 Altamirano, D., Belloni, T., Linares, M., van der Klis, M.,
1165 Wijnands, R., Curran, P. A., Kalamkar, M., Stiele, H., Motta,
1166 S., Muoz-Darias, T., Casella, P., Krimm, H. 2011c, *ApJ*, 742,
1167 L17

1168 Belloni, T., Homan, J., Casella, P., van der Klis, M., Nespoli, E.,
1169 Lewin, W. H. G., Miller, J. M., & Méndez, M. 2005, *A&A*, 440,
1170 207

1171 Belloni, T., Klein-Wolt, M., Méndez, M., van der Klis, M. & van
1172 Paradijs, J. 2000, *A&A*, 355, 271

1173 Bhattacharyya, S., 2010, *AdSpR*, 45, 949

1174 Bodaghee, A., Rahoui, F., Tomsick, J. A., Rodriguez, J., 2012,
1175 *ApJ*, 751, 113

1176 Burrows, David N., Hill, J. E., Nousek, J. A., Kennea, J. A.,
1177 Wells, A., Osborne, J. P., Abbey, A. F., Beardmore, A. et al.,
1178 2005, *Space Sc. Rev.*, 120, 165

1179 Caballero-García, M. D., Miller, J. M., Trigo, M. Díaz, Kuulkers,
1180 E., Fabian, A. C., Mas-Hesse, J. M., Steeghs, D. & van der
1181 Klis, M. 2009, *ApJ*, 692, 1339

1182 Capitanio, F., Del Santo, M., Bozzo, E., Ferrigno, C., De Cesare,
1183 G., & Paizis, A., 2012, *MNRAS*, 422, 3130

1184 Capitanio, F., Tramacere, A., Del Santo, M., Bozzo, E.,
1185 Watanabe, K., Caballero, I., Chenevez, J., Paizis, A. et al.
1186 2011, *Astron. Telegram*, 3159, 1

1187 Capitanio, F., Giroletti, M., Molina, M., Bazzano, A., Tarana, A.,
1188 Kennea, J., Dean, A. J., Hill, A. B. et al. 2009, *ApJ*, 690, 1621

1189 Capitanio, F., Bazzano, A., Ubertini, P., Zdziarski, A. A., Bird,
1190 A. J., De Cesare, G., Dean, A. J., Stephen, J. B. & Tarana, A.
1191 2006, *ApJ*, 643, 376

1192 Casella, P., Belloni, T. & Stella, L., 2005, *ApJ*, 629, 403

1193 Castro-Tirado, A. J., Brandt, S., Lund, N., Lapshev, I., Sunyaev,
1194 R. A., Shlyapnikov, A. A., Guziy, S. & Pavlenko, E. P. 1994,
1195 *ApJS*, 92, 469

1196 Chaty, S., Rahoui, F., Foellmi, C., Tomsick, J. A., Rodriguez, J.
1197 & Walter, R. 2008, *A&A*, 484, 783

1198 Del Santo, M., Belloni, T. M., Homan, J., Bazzano, A., Casella,
1199 P., Fender, R. P., Gallo, E., Gehrels, N. et al. 2009, *MNRAS*,
1200 392, 992

1201 Del Santo, M., Kuulkers, E., Bozzo, E., Capitanio, F.,
1202 Alfonso-Garzon, J., Beckmann, V., Bird, T., Brandt, S. et al.
1203 2011, *Astron. Telegram*, 3203, 1

1204 Dunn, R. J. H., Fender, R. P., Kórding, E. G., Cabanac, C. &
1205 Belloni, T. 2008, *MNRAS*, 387, 545

1206 Eikenberry, S. S., Matthews, K., Murphy, T. W., Jr., Nelson, R.
1207 W., Morgan, E. H., Remillard, R. A. & Muno, M. 1998, *ApJ*,
1208 506, L31

1209 Fender, R. P., Belloni, T. M., Gallo, E., 2004, *MNRAS*, 355, 1105

1210 Frank, J., King, A., Raine, D., 2002, *Accretion Power in*
1211 *Astrophysics*, 3rd Edition, Cambridge University Press

1212 Fujimoto, M. Y., Hanawa, T., & Miyaji, S., 1981, *ApJ*, 247, 267

1213 Greiner, J., 1994, *AGAb*, 10, 23

1214 Homan, J., Belloni, T., 2005, *Ap&SS*, 300, 107

1215 In't Zand, J. J. M., Heise, J., Lowes, P., & Ubertini, P. 2003,
1216 *Astron. Telegram*, 160, 1

1217 Jahoda, K., Swank, J. H., Giles, A. B., Stark, M. J., Strohmayer,
1218 T., Zhang, WT., & Morgan, E. H. 1996, *SPIE*, 2808, 59

1219 Janiuk, A., Misra, R., 2012, *A&A*, 540, 114

1220 Joint, A., Jourdain, E., Malzac, J., Roques, J. P., Corbel, S.,
1221 Rodriguez, J. & Kalemci, E. 2007, *ApJ*, 657, 400

1222 Klein-wolt, M., et al., 2002, *MNRAS*, 331, 745

1223 Krimm, H. A. & Kennea, J. A. 2011, *Astron. Telegram*, 3148, 1

1224 Krimm, H. A., Barthelmy, S. D., Baumgartner, W., Cummings,
1225 J., Fenimore, E., Gehrels, N., Kennea, J. A., Markwardt, C. B.
1226 et al. 2011, *Astron. Telegram*, 3144, 1

1227 King, A. L., Miller, J. M., Raymond, J., Fabian, A. C., Reynolds,
1228 C. S., Kallman, T. R., Maitra, D., Cackett, E. M., Rupen, M.
1229 P., 2012, *ApJL*, 746, 20

1230 Kuulkers, E., Lutovinov, A., Parmar, A., Capitanio, F., Mowlavi,
1231 N. & Hermsen, W. 2003, *Astron. Telegram*, 149, 1

1232 Kubota, A., Tanaka, Y., Makishima, K., Ueda, Y., Dotani, T.,
1233 Inoue, H., Yamaoka, K., 1998, *PASJ*, 50, 667

1234 Lewin, W. H. G., van Paradijs, J., & Taam, R. E. 1995, in *X-Ray*
1235 *Binaries*, ed. W. H. G. Lewin, J. van Paradijs, & E. P. J. van
1236 den Heuvel (Cambridge: Cambridge Univ. Press), 175

1237 Lochner, J., Whitlock, L., Kouveliotou, C., 1992, *IAUC*, 5658, 2

1238 Lutovinov, A. A., Revnivtsev, M., Molkov, S. & Sunyaev, R.
1239 2005, *A&A*, 430, 997

1240 Lutovinov, A. A. & Revnivtsev, M. G. 2003, *Astron. Lett.*, 29, 719

1241 Markoff, S., Nowak, M. A., & Wilms, J. 2005, *ApJ*, 635, 1203

1242 Massaro, E., Ventura, G., Massa, F., Feroci, M., Mineo, T.,
1243 Cusumano, G., Casella, P. & Belloni, T. 2010, *A&A*, 513, 21

1244 Miller, J. M. 2007, *ARA&A*, 45, 441

1245 Mineo, T., Romano, P., Mangano, V., Moretti, A., Cusumano,
1246 G., La Parola, V., Troja, E., Campana, S. et al., 2006, *Nuovo*
1247 *Cimento B*, 121, 1521

1248 Mirabel, I. F., Dhawan, V., Chaty, S., Rodriguez, L. F., Marti, J.,
1249 Robinson, C. R., Swank, J., & Geballe, T., 1998, *A&A*, 330, L9

1250 Mirabel, I. F. & Rodriguez, L. F. 1994, *Nature*, 371, 46

1251 Muno, M. P., Morgan, E. H. & Remillard, R. A., 1999, *ApJ*, 527,
1252 321

1253 Munóz-Darias, T., Casares, J., & Martínez-Pais, I. G. 2008,
1254 *MNRAS*, 385, 2205

1255 Neilsen, J., Remillard, R. A., Lee, J. C., 2012, *ApJ*, 750, 71

1256 Pahari, M., et al., 2013a, *ApJ*, 778, 46

1257 Pahari, M., et al., 2013b, *MNRAS*, 436, 2334

1258 Pahari, M., et al., 2013c, *ApJ*, 778, 136

1259 Pahari, M., Bhattacharyya, S., Yadav, J. S. & Pandey, S. K.,
1260 2011, *MNRAS*, 422, L87

1261 Pahari, M., Bhattacharyya, S. & Yadav, J. S. 2011, *Astron.*
1262 *Telegram*, 3266, 1

1263 Pahari, M. & Pal, S. 2010, *MNRAS*, 409, 903

1264 Paul, B., Agrawal, P. C., Rao, A. R., Vahia, M. N., Yadav, J. S.,
1265 Marar, T. M. K., Seetha, S. & Kasturirangan, K. 1998, *A&AS*,
1266 128, 145

1267 Rao, A. R., Yadav, J. S. & Paul, B., 2000, *ApJ*, 544, 443

1268 Rebusco, P., Moskalik, P., Kluzniak, W., Abramowicz, M. A.,
1269 2012, *A&A*, 540, L4

1270 Reig, P., Belloni, T., van der Klis, M., Méndez, M., Kylafis, N.
1271 D., & Ford, E. C., 2000, *ApJ*, 541, 883

1272 Remillard, R. A. & McClintock, J. E., 2006, *ARA&A*, 44, 49

1273 Rodriguez, J., Corbel, S., Tomsick, J. A., Paizis, A. & Kuulkers,
1274 E. 2011a, *Astron. Telegram*, 3168, 1 F

1275 Rodriguez, J., Corbel, S., Caballero, I., Tomsick, J. A., Tzioumis,
1276 T., Paizis, A., Cadolle, Bel M., & Kuulkers, E., 2011b, *A&A*,
1277 533, L4

1278 Rothschild, R. E., Blanco, P. R., Gruber, D. E., Heindl, W. A.,
1279 MacDonald, D. R., Marsden, D. C., Pelling, M. R., Wayne, L.
1280 R. & Hink, P. L. 1998, *ApJ*, 496, 538

1281 Shaposhnikov, Nikolai 2011, *Astron. Telegram*, 3179, 1

1282 Sheskin, D. J., 2003, *Handbook of Parametric and Nonparametric*
1283 *Statistical Procedures: Third Edition*, CRC Press

1284 Soleri, P., Belloni, T. & Casella, P. 2008, *MNRAS*, 383, 1089

1285 Steeghs, D., McClintock, J. E., Parsons, S. G., et al., 2013, *ApJ*,
1286 768, 185

1287 Sunyaev, R. & Revnivtsev, M., 2000, *A&A*, 358, 617

1288 Taam, R. E., Xingming, C. & Swank, J., E. 1997, *APJ*, 485, L83

1289 Tingay, S. J., Jauncey, D. L., Preston, R. A., Reynolds, J. E.,
1290 Meier, D. L., Murphy, D. W., Tzioumis, A. K., McKay, D. J. et
1291 al. 1995, *Nature*, 374, 141

1292 Yadav, J. S., Rao, A. R., Agrawal, P. C., Paul, B., Seetha, S. &
1293 Kasturirangan, K. 1999, *ApJ*, 517, 935

1294 Yadav, J. S., 2001, *ApJ*, 548, 876

1295 Yadav, J. S., 2006, *ApJ*, 646, 385

1296 Yadav, J. S., & Pahari, M., 2013, under preparation

1297 Zdziarski, A. A. & Gierliński, M. 2004, *Prog. Theor. Phys.*
1298 *Suppl.*, 155, 99

TABLE 1
OBSERVATIONAL DETAILS OF IGR J17091–3624 USING *RXTE*/PCA AND *SWIFT*/XRT DATA DURING 2011 OUTBURST.

Observation date (DD-MM-YY)	MJD	Instrument	Observation ID	Good time interval (sec)	Average soft color	Average hard color	spectral state/class	PDS features
09-02-11	55601.06	XRT(WT)	00031921005	1467.4	–	–	LS?	band-limited noise observed
10-02-11	55602.58	XRT(WT)	00031921006	2200.4	–	–	LS?	strong band-limited noise (rms amplitude(%) 9.4 ± 0.6)
12-02-11	55604.21	XRT(WT)	00031921008	2198.1	–	–	LS?	band-limited noise observed
13-02-11	55605.21	XRT(WT)	00031921009	2151.2	–	–	LS?	band-limited noise observed
14-02-11	55606.16	XRT(WT)	00031921010	1877.6	–	–	LS?	band limited noise observed
15-02-11	55607.23	XRT(WT)	00031921011	2101.6	–	–	LS	band-limited noise & a break in PDS is observed ($\sim 0.19 \pm 0.03$ Hz)
16-02-11	55608.23	XRT(WT)	00031921012	2182.3	–	–	LS	band-limited noise & broad QPO-like and feature observed (0.18±0.02 Hz, 2.37±0.18, 13.9±2.6)
18-02-11	55610.17	XRT(WT)	00031921013	2176.5	–	–	LS	strong band-limited noise & broad QPO-like and feature observed (0.22±0.03 Hz, 2.25±0.18, 8.7±1.3)
20-02-11	55612.25	XRT(WT)	00031921014	2104.2	–	–	HIMS	pds fitted with (lore+bknpower)(122.1/125), type-C QPO (0.51±0.13 Hz, 5.25±0.12, 12.8±0.6) and flat top noise ($\sim 7\%$) detected
22-02-11	55614.19	XRT(WT)	00031921015	2050.2	–	–	SIMS	broad Lorentzian (~ 1.89 Hz) and weak red noise detected
23-02-11	55615.99	PCA	96065-03-01-03	3184.4	0.73±0.01	0.36±0.02	SIMS	pds fitted with (lore+bknpower)(225.9/224), transient type-B QPO (4.16±0.08 mHz, 5.71±0.34, 6.68±0.79) with weak red noise (rms amplitude(%) 4.25±0.18)
24-02-11	55616.25	XRT(WT)	00031921016	1065.6	–	–	SIMS	pds fitted with (lore+lore+bknpower)(117.3/122), transient type-B QPO (4.32±0.37 Hz, 7.17±0.36, 5.28±0.32) broad Lorentzian noise (0.83±0.14 Hz, 7.82±0.27)
26-02-11	55619.01	PCA	96065-03-02-00	1712.2	0.75±0.01	0.41±0.02	HIMS	pds fitted with (lore+bknpower)(213.5/224), type-C QPO (3.73±0.09 Hz, 4.76±0.14, 16.9±0.6) with strong flat-top noise (rms amplitude(%) 7.85±0.18)
28-02-11	55621.34	XRT(WT)	00031921017	2576.6	–	–	SIMS	pds fitted with (lore+bknpower)(121.8/125), transient type-B QPO (3.84±0.11 Hz, 6.79±0.23, 5.31±0.55) with weak red noise (rms amplitude(%) 3.96±0.49)
02-03-11	55622.59	PCA	96420-01-01-00	3744.3	0.72±0.04	0.39±0.08	HIMS	pds fitted with (lore+bknpower)(234.2/224), type-C QPO (3.67±0.26 Hz, 4.17±0.56, 21.3±0.5) with strong flat-top noise (rms amplitude(%) 8.19±0.47)
03-03-11	55623.28	PCA	96420-01-01-01	2064.5	0.68±0.03	0.36±0.02	SIMS	pds fitted with (lore+bknpower)(229.9/224), transient type-B QPO (4.85±0.08 Hz, 7.67±0.68, 6.14±0.29) with weak red noise (rms amplitude(%) 3.43±0.59)
03-03-11	55623.86	PCA	96420-01-01-02	6944.4	0.66±0.02	0.38±0.03	SIMS	pds fitted with (lore+bknpower)(212.6/224), type-B/type-C QPO (5.32±0.46 Hz, 6.38±0.56, 6.31±0.37) with flat-top noise (rms amplitude(%) 6.58±0.79)
04-03-11	55624.56	PCA	96420-01-02-00	1584.2	0.62±0.03	0.33±0.01	SIMS to HIMS transition	pds fitted with (lore+bknpower)(217.3/224), transient type-C QPO (5.15±0.11 Hz, 4.98±0.27, 9.11±0.09) with strong flat-top noise (rms amplitude(%) 7.12±0.35)
04-03-11	55624.85	XRT(WT)	00031921020	2289.6	–	–	HIMS	pds fitted with (lore+bknpower)(226.4/224), transient type-C QPO (5.40±0.23 Hz, 4.85±0.39, 8.87±0.69) with strong flat-top noise (rms amplitude(%) 7.12±0.35)
06-03-11	55626.39	PCA	96420-01-02-01	65.5	0.67±0.03	0.35±0.01	HIMS	pds fitted with (lore+bknpower)(218.1/224), transient type-C QPO (5.23±0.09 Hz, 5.31±0.23, 10.9±0.7) with strong flat-top noise (rms amplitude(%) 8.89±0.49)
06-03-11	55626.23	XRT(WT)	00031921022	1704.1	–	–	HIMS	pds fitted with (lore+bknpower)(229.6/224), narrow, weak QPO-like feature (0.68±0.03 Hz, 12.5±0.4, 3.08±0.11) with weak red noise (rms amplitude(%) 5.15±0.26)
08-03-11	55628.47	PCA	96420-01-02-02	3202.2	0.64±0.01	0.36±0.01	HIMS	no QPO is detected and weak red noise observed (rms amplitude(%) 2.55±0.34)
08-03-11	55628.23	XRT(WT)	00031921022	1704.1	–	–	HIMS	pds fitted with (lore+lore+bknpower)(231.8/221), characteristic QPO (11.5±0.8 mHz, 4.46±0.58, 5.72±0.18), narrow, weak QPO-like feature (2.61±0.12 Hz, 11.8±0.7, 2.97±0.23) with weak red noise (rms amplitude(%) 3.69±0.25)
10-03-11	55630.84	PCA	96420-01-02-03	1648.8	0.67±0.02	0.37±0.04	HIMS	pds fitted with (lore+bknpower)(118.3/125), transient type-B QPO (4.46±0.21 Hz, 6.09±0.53, 7.81±0.86) with weak red noise (rms amplitude(%) 2.99±0.35)
10-03-11	55630.16	XRT(WT)	00031921023	1401.5	–	–	HIMS	pds fitted with (lore+bknpower)(114.6/125), characteristic QPO (13.3±1.4 mHz, 8.6±2.3, 7.39±0.41) with weak red noise (rms amplitude(%) 3.65±0.33)
12-03-11	55632.54	PCA	96420-01-03-00	1520.4	0.63±0.02	0.33±0.02	SIMS	pds fitted with (lore+lore+bknpower)(212.6/221), heartbeat ν_f (29.6±1.2 mHz, 7.42±0.51, 28.6±1.8) heartbeat ν_{h1} (62.4±4.5 mHz, 5.56±0.36, 9.02±0.48) heartbeat ν_{h2} (0.11±0.05 Hz, 5.77±0.42, 4.26±0.53)
12-03-11	55632.73	XRT(WT)	00031921024	2182.3	–	–	SIMS	pds fitted with (lore+lore+bknpower)(223.6/218), heartbeat ν_f (31.2±2.3 mHz, 18.6±2.2, 25.9±1.8) heartbeat ν_{h1} (63.4±4.8 mHz, 4.84±0.24, 7.77±0.83) heartbeat ν_{h2} (0.11±0.08 Hz, 2.77±0.12, 6.45±0.34)
13-03-11	55633.24	XRT(WT)	00031921025	2009.8	–	–	SIMS	
14-03-11	55634.72	PCA	96420-01-03-01	3344.2	0.53±0.02	0.28±0.06	IVS	
15-03-11	55635.65	XRT(WT)	00031921026	1481.2	–	–	SIMS	
18-03-11	55638.54	XRT(WT)	00031921029	2164.6	–	–	IVS	
19-03-11	55639.71	PCA	96420-01-04-00	2752.3	0.50±0.01	0.21±0.01	variable state/ ρ class	
19-03-11	55639.67	XRT(WT)	00031921028	2631.5	–	–	variable state/ ρ class	
20-03-11	55640.47	XRT(WT)	00031921030	2352.5	–	–	variable state/ ρ class	

NOTE. — Continuation of Table 1 ...

Observation date (DD-MM-YY)	MJD	Instrument	Observation ID	Good time interval (sec)	Average soft color	Average hard color	spectral state/class	PDS features
22-03-11	55642.20 55642.35	PCA XRT(WT)	96420-01-04-02 00031921031	2976.4 2260.3	0.54±0.01 –	0.29±0.09 –	variable state/ ρ class	pds fitted with (1ore+1ore+1ore+bknpower)(228.6/218), heartbeat ν_f (25.5±1.4 mHz, 9.69±0.74, 22.0±1.6) heartbeat ν_{h1} (51.7±2.4 mHz, 5.29±0.33, 9.39±0.88) transient type-B QPO (2.73±0.15 Hz, 8.36±2.43, 3.16±0.22)
23-03-11	55643.78	PCA	96420-01-04-01	1152.4	0.55±0.11	0.34±0.03	IVS	pds fitted with (1ore+bknpower)(233.4/224), characteristic QPO (12.7±1.1 mHz, 11.6±1.6, 6.87±0.49) with weak red noise (rms amplitude(%) 2.67±0.19)
24-03-11	55644.75	PCA	96420-01-04-03	2752.8	0.57±0.03	0.33±0.04	IVS	pds fitted with (1ore+1ore+1ore+bknpower)(227.5/218), ν_f (11.6±0.9 mHz, 2.89±0.16, 6.02±0.39) broad Lorentzian noise (60.1±3.7 mHz, 4.15±0.21) and transient type-A QPO (8.18±0.62 Hz, 3.75±0.29, 5.26±0.18)
25-03-11	55645.86	PCA	96420-01-05-02	3312.3	0.58±0.01	0.37±0.05	SIMS	pds fitted with (1ore+bknpower)(214.4/224), transient type-A QPO (7.78±0.45 Hz, 4.28±0.87, 4.57±0.29) with weak red noise (rms amplitude(%) 4.13±1.16)
26-03-11	55646.89	XRT(WT)	00031921034	2160.1	–	–	IVS	pds fitted with (1ore+bknpower)(123.8/125), characteristic QPO (14.1±0.2 mHz, 8.97±1.1, 6.10±0.66) with weak red noise (rms amplitude(%) 3.23±0.26)
27-03-11	55648.01	PCA	96420-01-05-00	32990.4	0.52±0.04	0.27±0.03	variable state/ ρ class	pds fitted with (1ore+1ore+1ore+bknpower)(228.4/218), heartbeat ν_f (21.1±1.4 mHz, 14.8±1.1, 13.3±1.2) heartbeat ν_{h1} (44.2±2.9 mHz, 13.3±1.2, 4.89±0.57) heartbeat ν_{h2} (85.6±5.5 mHz, 16.8±1.5, 6.15±0.74)
29-03-11	55649.06	PCA	96420-01-05-03	2640.3	0.55±0.01	0.33±0.02	variable state/ ρ class	pds fitted with (1ore+1ore+bknpower)(232.7/221), heartbeat ν_f (23.8±1.9 mHz, 5.39±0.69, 15.9±1.4) heartbeat ν_{h1} (49.7±2.2 mHz, 11.8±3.6, 6.89±0.56)
30-03-11	55650.98 55650.74	PCA XRT(WT)	96420-01-05-01 00031921036	2304.5 331.65	0.48±0.02 –	0.28±0.02 –	variable state/ ρ class	pds fitted with (1ore+1ore+1ore+bknpower)(213.5/218), heartbeat ν_f (24.1±1.6 mHz, 13.5±0.3, 15.9±1.4) heartbeat ν_{h1} (50.6±2.8 mHz, 16.8±0.6, 7.88±0.71) heartbeat ν_{h2} (75.7±5.3 mHz, 9.54±0.93, 5.06±0.48)
31-03-11	55651.88	PCA	96420-01-05-04	3968.1	0.51±0.02	0.35±0.04	variable state/ ρ class	pds fitted with (1ore+1ore+1ore+bknpower)(222.8/218), heartbeat ν_f (26.3±1.4 mHz, 14.1±0.5, 16.8±1.7) heartbeat ν_{h1} (52.8±3.9 mHz, 12.7±0.3, 7.53±1.05) heartbeat ν_{h2} (79.6±4.4 mHz, 9.41±0.23, 9.19±1.16) transient type-A QPO (8.36±0.26 Hz, 4.79±0.38, 3.66±0.31)
02-04-11	55653.70	PCA	96420-01-06-00	3488.7	0.50±0.01	0.29±0.01	variable state/ ρ class	pds fitted with (1ore+1ore+1ore+bknpower)(226.5/218), heartbeat ν_f (33.6±1.3 mHz, 11.2±0.3, 22.3±1.3) heartbeat ν_{h1} (67.8±2.6 mHz, 5.84±0.21, 10.9±2.6) heartbeat ν_{h2} (0.11±0.01 Hz, 3.19±0.17, 6.23±0.13)
03-04-11	55654.89	PCA	96420-01-06-01	6112.3	0.53±0.01	0.31±0.04	variable state/ ρ class	pds fitted with (1ore+1ore+1ore+1ore+bknpower)(207.4/215), heartbeat ν_f (36.6±0.7 mHz, 9.95±0.54, 29.3±1.3) heartbeat ν_{h1} (75.9±4.1 mHz, 4.21±0.19, 15.3±1.1) broad Lorentzian noise (0.21±0.05 Hz, 9.83±0.79) transient type-A QPO (7.28±0.14 Hz, 3.21±0.17, 4.89±0.14)
05-04-11	55656.71	PCA	96420-01-06-02	5136.3	0.54±0.01	0.27±0.04	variable state/ ρ class	pds fitted with (1ore+1ore+bknpower)(231.5/221), heartbeat ν_f (39.1±1.6 mHz, 6.89±0.32, 32.5±2.2) heartbeat ν_{h1} (81.3±3.8 mHz, 3.95±0.23, 14.9±1.4)
06-04-11	55657.31	PCA	96420-01-06-03	1812.8	0.55±0.01	0.25±0.02	variable state/ ρ class	pds fitted with (1ore+1ore+1ore+bknpower)(225.8/218), heartbeat ν_f (35.8±2.1 mHz, 4.56±0.19, 14.5±1.6) heartbeat ν_{h1} (64.8±4.7 mHz, 4.80±0.13, 23.6±1.1) transient type-B QPO (4.02±0.12 Hz, 2.15±0.17, 13.9±0.8)
10-04-11	55661.75	PCA	96420-01-07-00	3376.6	0.58±0.01	0.28±0.03	variable state/ ρ class	pds fitted with (1ore+1ore+1ore+bknpower)(230.3/218), heartbeat ν_f (45.9±2.1 mHz, 8.47±0.76, 33.8±1.6) heartbeat ν_{h1} (94.2±3.4 mHz, 9.33±0.36, 11.6±1.7) transient type-A QPO (7.76±0.35 Hz, 2.48±0.22, 7.53±0.45)
11-04-11	55662.56	PCA	96420-01-07-01	3375.2	0.56±0.01	0.27±0.02	variable state/ ρ class	pds fitted with (1ore+1ore+1ore+bknpower)(210.7/218), heartbeat ν_f (45.2±0.7 mHz, 4.61±0.25, 31.8±2.2) heartbeat ν_{h1} (90.4±3.5 mHz, 3.22±0.25, 11.2±0.9) broad Lorentzian noise (5.52±1.38 Hz, 9.98±1.13)
12-04-11	55663.34	PCA	96420-01-07-02	3278.5	0.58±0.01	0.28±0.02	variable state/ ρ class	pds fitted with (1ore+1ore+1ore+bknpower)(224.4/218), heartbeat ν_f (44.5±0.6 mHz, 2.69±0.13, 30.4±1.7) heartbeat ν_{h1} (90.1±0.2 mHz, 13.8±1.6, 8.63±0.73) transient type-B QPO (4.93±0.09 Hz, 2.46±0.22, 4.39±0.11)
15-04-11	55666.55	PCA	96420-01-08-00	1513.6	0.59±0.03	0.29±0.03	ρ to other class transition (may be κ/λ)	pds fitted with (1ore+1ore+1ore+bknpower)(211.6/218), broad Lorentzian noise (56.73±3.43 mHz, 30.1±2.4), broad Lorentzian noise (0.22±0.07 Hz, 19.4±1.5) and broad QPO-like feature (3.09±0.05 Hz, 3.25±0.36, 9.65±1.23)

NOTE. — LS, HIMS, SIMS & IVS stand for the low/hard state, Hard intermediate state, soft intermediate state and Intermediate variable state respectively. In the last column, quantities in braces for quasi-periodic oscillations (QPOs) represent (frequency with error, q-factor with error, rms amplitude with error) and for noise components (frequency with error, rms with error). ν_f , ν_{h1} and ν_{h2} represent fundamental QPO of ρ -like/variable state oscillations, its first and second harmonics respectively. Models used to fit PDS and χ^2/dof are also provided.

TABLE 2

BEST FIT PARAMETERS (WITH 1σ ERROR BARS) OBTAINED BY FITTING THE LOW/HARD STATE, HARD INTERMEDIATE AND SOFT INTERMEDIATE STATE SPECTRA OF IGR J17019–3624 WITH THE **powerlaw** AND THE **diskbb+powerlaw** MODELS RESPECTIVELY.

Instrument used	Observation ID	Date (DD-MM-YY)	state/class	Γ	kT_{in} (keV)	N_{diskbb}	Flux _{total}	Flux _{powerlaw}	Flux _{diskbb}	χ^2/dof
XRT	00031921005	09-02-11	LS?	$1.66^{+0.05}_{-0.04}$	–	–	0.61	–	–	657.98/632
XRT	00031921006	10-02-11	LS?	$1.75^{+0.05}_{-0.04}$	–	–	0.45	–	–	573.58/632
XRT	00031921008	12-02-11	LS?	$1.63^{+0.03}_{-0.03}$	–	–	0.87	–	–	728.57/632
XRT	00031921009	13-02-11	LS?	$1.69^{+0.03}_{-0.04}$	–	–	0.98	–	–	667.64/632
XRT	00031921010	14-02-11	LS?	$1.73^{+0.04}_{-0.05}$	–	–	0.71	–	–	694.01/632
XRT	00031921011	15-02-11	LS	$1.67^{+0.03}_{-0.04}$	–	–	0.95	–	–	726.74/632
XRT	00031921012	16-02-11	LS	$1.62^{+0.03}_{-0.03}$	–	–	1.11	–	–	629.34/632
XRT	00031921013	18-02-11	LS	$1.66^{+0.03}_{-0.03}$	–	–	1.03	–	–	586.28/632
XRT	00031921014	20-02-11	HIMS	$1.79^{+0.04}_{-0.05}$	–	–	0.98	–	–	609.43/632
XRT	00031921015	22-02-11	SIMS	$2.22^{+0.07}_{-0.05}$	$0.96^{+0.04}_{-0.06}$	$21.7^{+8.8}_{-4.6}$	2.47	1.85	0.63	595.40/632
PCA	96065-03-01-03	23-02-11	SIMS	$2.29^{+0.03}_{-0.03}$	$1.10^{+0.11}_{-0.06}$	$6.43^{+2.12}_{-1.45}$	0.79	0.68	0.11	45.12/42
PCA	96065-03-02-00	26-02-11	SIMS	$2.38^{+0.04}_{-0.07}$	$0.93^{+0.11}_{-0.06}$	$11.50^{+3.39}_{-3.50}$	0.68	0.59	0.08	43.59/42
PCA	96420-01-01-00	02-03-11	HIMS	$2.22^{+0.02}_{-0.03}$	$1.10^{+0.06}_{-0.04}$	$2.69^{+0.67}_{-0.52}$	0.47	0.43	0.04	44.52/42
PCA	96420-01-01-01	03-03-11	SIMS	$2.30^{+0.08}_{-0.03}$	$1.14^{+0.04}_{-0.09}$	$4.36^{+0.56}_{-0.48}$	0.49	0.40	0.09	39.42/42
PCA	96420-01-01-02	03-03-11	SIMS	$2.41^{+0.04}_{-0.03}$	$0.82^{+0.10}_{-0.03}$	$6.08^{+3.25}_{-2.46}$	0.35	0.33	0.02	40.78/42
PCA	96420-01-02-00	04-03-11	SIMS/HIMS	$2.39^{+0.03}_{-0.06}$	$1.23^{+0.03}_{-0.02}$	$12.30^{+1.93}_{-1.95}$	1.81	1.48	0.33	31.89/42
PCA	96420-01-02-01	06-03-11	HIMS	$2.44^{+0.06}_{-0.06}$	$1.15^{+0.12}_{-0.12}$	$16.30^{+3.35}_{-3.36}$	1.83	1.50	0.33	33.58/42
PCA	96420-01-02-02	08-03-11	HIMS	$2.34^{+0.04}_{-0.03}$	$1.24^{+0.02}_{-0.03}$	$13.87^{+1.33}_{-1.34}$	1.77	1.46	0.31	40.75/42
PCA	96420-01-02-03	10-03-11	HIMS	$2.39^{+0.03}_{-0.06}$	$1.23^{+0.03}_{-0.02}$	$10.97^{+1.32}_{-1.93}$	1.72	1.42	0.29	41.17/42
PCA	96420-01-03-00	12-03-11	SIMS	$2.47^{+0.03}_{-0.06}$	$0.89^{+0.08}_{-0.07}$	$4.47^{+1.15}_{-0.85}$	0.31	0.28	0.03	42.12/42
PCA	96420-01-05-02	25-03-11	SIMS	$2.34^{+0.02}_{-0.03}$	$1.15^{+0.04}_{-0.06}$	$20.6^{+2.11}_{-1.37}$	1.75	1.23	0.51	43.78/42

NOTE. — Γ is the power-law index, kT_{in} is temperature of the inner disk edge in units of keV and N_{diskbb} is the disk blackbody model normalization. Flux_{total} is the total flux, Flux_{diskbb} is the flux of the disk component and Flux_{powerlaw} is the flux of the power-law component. All the fluxes are calculated in the energy range 2.0-60.0 keV for combined PCA and *SWIFT*/XRT spectra and 0.3-10.0 keV for *SWIFT*/XRT spectra only. Fluxes are given in a unit of 10^{-9} ergs/s/cm².

TABLE 3

SUMMARY OF COMPARATIVE STUDY OF SOME CHARACTERISTIC PARAMETERS OF IGR J17091–3624 AND GRS 1915+105.

Characteristic parameters	IGR J17091–3624 (variable state/ ρ -like class)	GRS 1915+105 (ρ' class)
Oscillation timescale	~ 20 s – 50 s	~ 40 s – 110 s
Change in timescale	increases with time ~ 1.32 mHz/day	increases with time ~ 0.36 mHz/day
Peak to minimum flux ratio	~ 2.91 – 3.82	~ 3.38 – 4.28
X-ray flux and hard color relation	strong anti-correlation found	strong anti-correlation found
Variability pattern (fitting with $f(t)=ae^{t/t_i}$)	slow exponential rise ($t_i=t_{rise} \sim 14.67$) fast decay ($t_i=t_{fall} \sim -3.62$)	slow exponential rise ($t_i=t_{rise} \sim 13.68$) fast decay ($t_i=t_{fall} \sim -2.48$)
QPOs	26.3 mHz, 52.8 mHz (on 31 Mar. 11) 36.6 mHz, 75.9 mHz (on 03 Apr. 11) 45.9 mHz, 94.2 mHz (on 10 Apr. 11) etc.	9.7 mHz & 19.2 mHz (on 26 May 97) 12.1 mHz & 24.3 mHz (on 03 Jun. 97) 18.5 mHz, 37.9 mHz (on 22 Jun. 97)

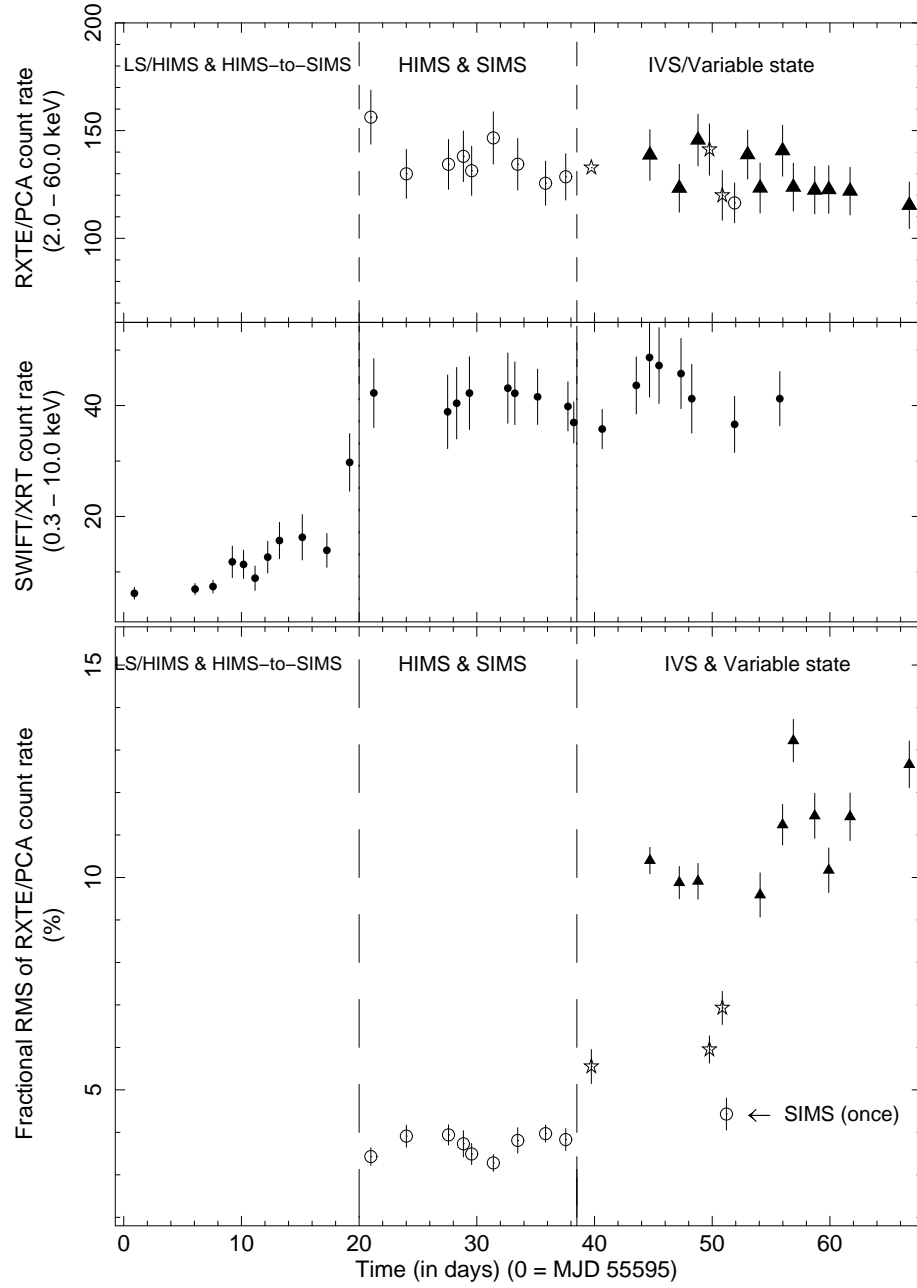


FIG. 1.— Overall nature of 2011 outburst of IGR paper J17091–3624. *Top panel:* plot of background-subtracted *RXTE/PCA* average count rate between 2.0–60.0 keV with time, *Middle panel:* simultaneous plot of background-subtracted *SWIFT/XRT* average count rate between 0.3–10.0 keV with time, *Bottom panel:* fractional RMS values of *RXTE/PCA* count rate as observed during LS, HIMS, SIMS and variable state/ ρ -like class. Due to contamination, *RXTE/PCA* has no data in first 20 days. HIMS & SIMS, Intermediate variable state and variable state observations are shown by open circles, stars and triangles respectively in the top and bottom panels. Vertical lines separate the LS/HIMS and the HIMS & SIMS and the variable state/ ρ -like class.

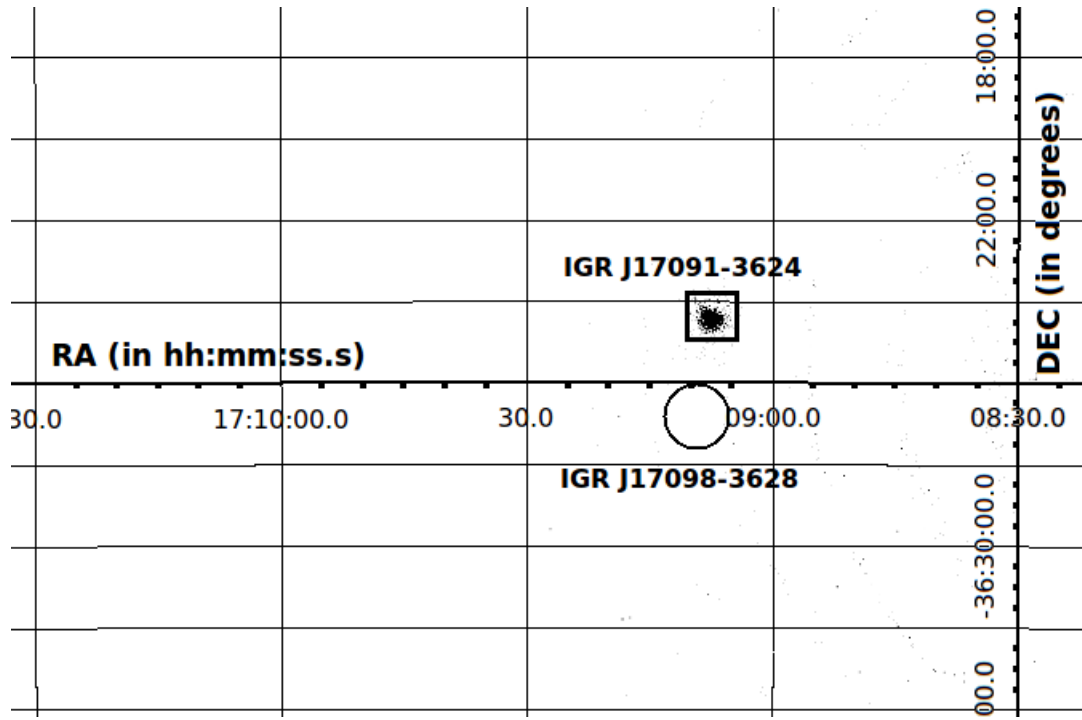


FIG. 2.— 0.3-10.0 keV filtered image of IGR J17091–3624 taken by the *SWIFT*/XRT in the photon counting mode on 03 February 11.

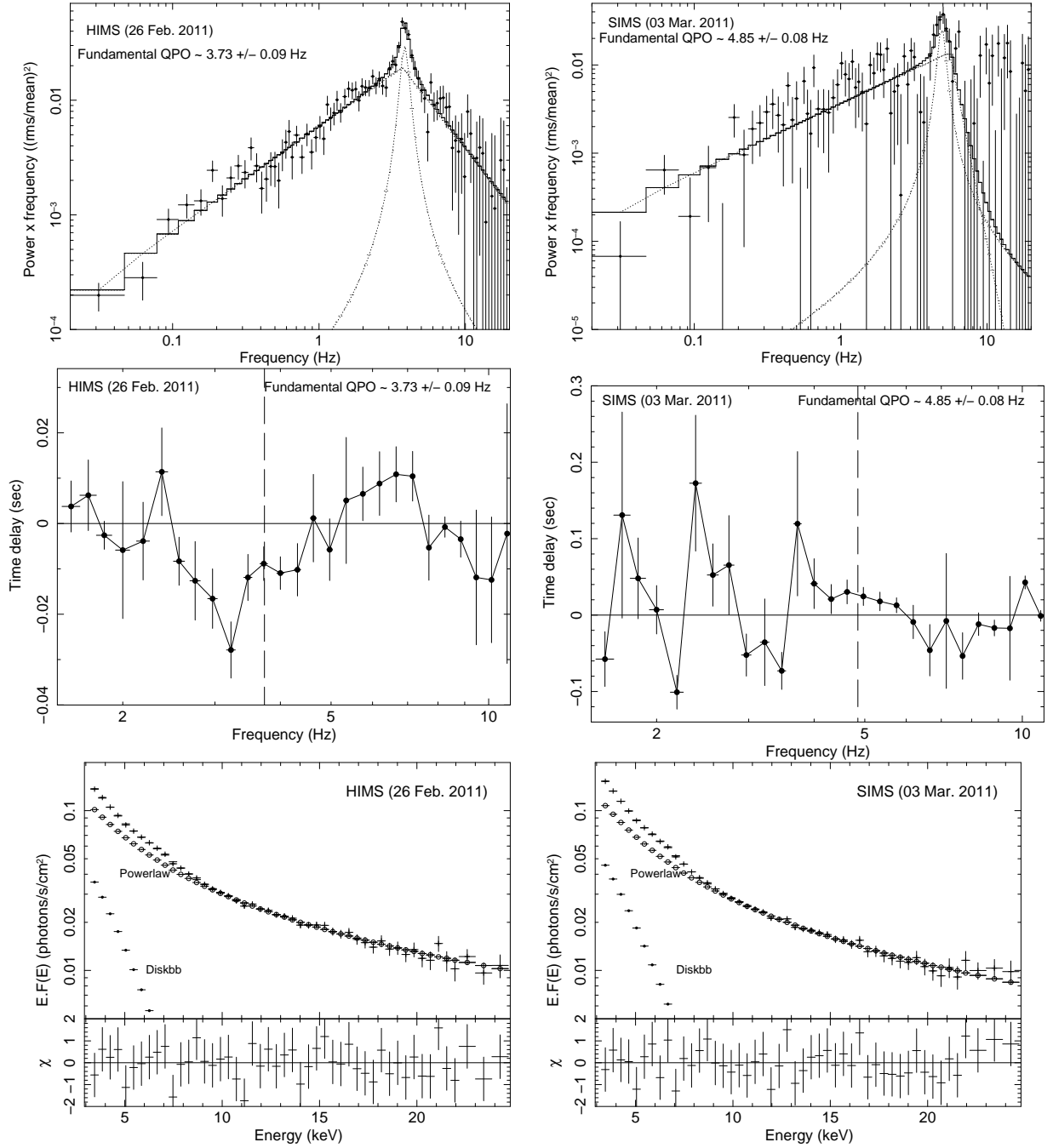


FIG. 3.— *SIMS* and *HIMS* in IGR J17091–3624 as observed by *RXTE/PCA*. Top panel : Power density spectra fitted with broken powerlaw and Lorentzians are shown during the hard intermediate state (*HIMS*) as observed on 26 February, 2011 (top left panel) and during soft intermediate state (*SIMS*) as observed on 03 March, 2011 (top right panel). Middle panel : frequency dependent time-lag spectra, calculated between 1.8–4.2 keV and 5.0–13.0 keV energy bands, are shown for same observations during the *HIMS* (middle left panel) and the *SIMS* (middle right panel). Dotted vertical lines show the fundamental QPO frequency in both panels. Bottom panels : *RXTE/PCA* spectra fitted with `diskbb+powerlaw` in the range 3.0–25.0 keV are shown for the *HIMS* (bottom left panel) and the *SIMS* (bottom right panel) along with their fitted model components and residuals.

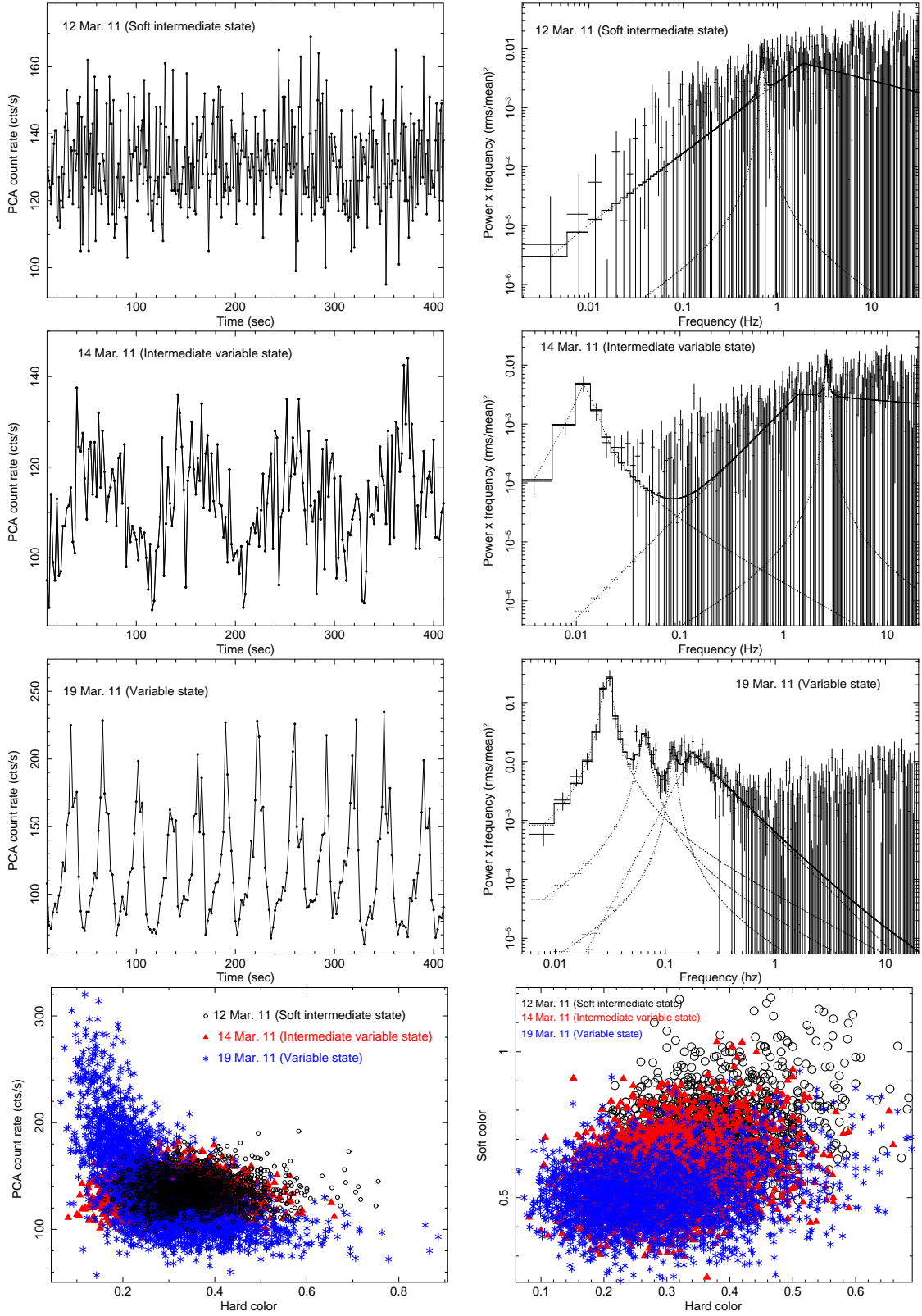


FIG. 4.— Transition from low-variability class (soft intermediate state) to high-variability class (variable state) via intermediate in IGR J17091–3624. Top three left panels show 2.0–60.0 keV *RXTE*/PCA light curves of the SIMS, IVS and Variable state respectively. Top three right panels show 2.0–60.0 keV *RXTE*/PCA rms normalized power density spectra of the SIMS, IVS and Variable state respectively, fitted with broken power-law and Lorentzian. *Bottom left and right panel:* evolution of classes from the SIMS to the variable state/ ρ -like class in the Hardness Intensity Diagram (HID) and the color color Diagram (CD) respectively. Each point in the HID and CD are created using 1 sec time binning for the entire observation and errors are $\leq 7\%$.

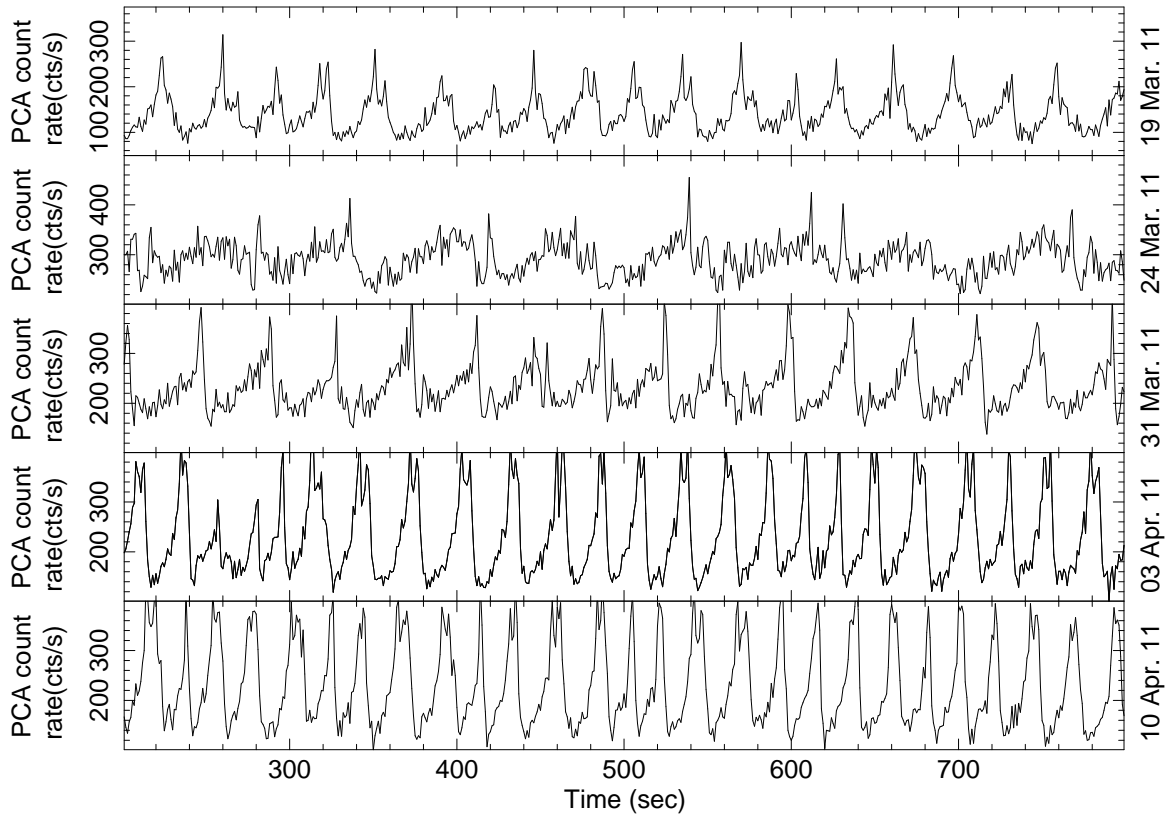


FIG. 5.— Lightcurve evolution of the variability pattern during variable state/ ρ -like class in IGR J17091–3624. All 5 panels show 2.0–60.0 keV background-subtracted PCA light curve for five different observations from 19 March 11 to 10 April 11 with 1s bintime.

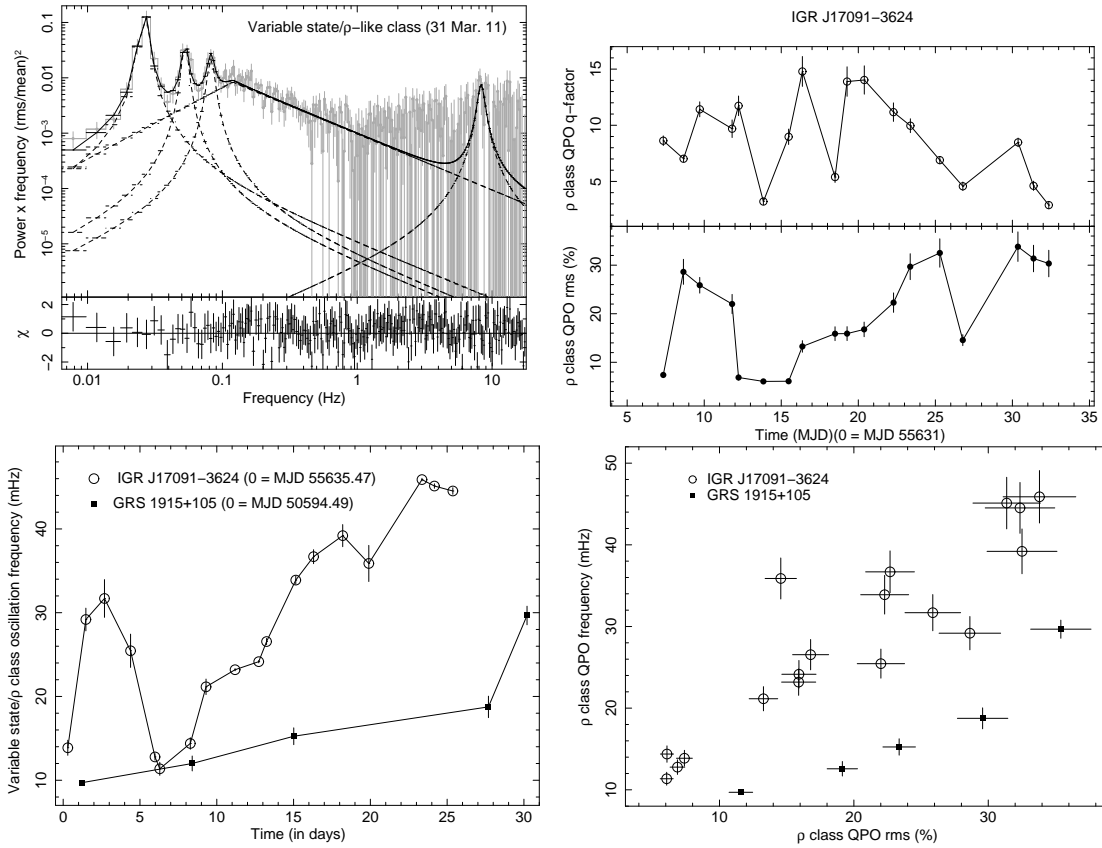


FIG. 6.— Power density spectral evolution during the variable state/ ρ -like class in IGR J17091-3624. Top left panel : Example of the PDS of a variability state/ ρ -like class, fitted with broken powerlaw and multiple Lorentzians (see Table 1 for parameter values) is shown as observed on 31 March, 2011. Fitted model components are shown in dotted lines alongwith the residuals. Top right panel : the time evolution of the quality factor and the rms amplitude(%) of the characteristic pulsation at the fundamental frequency during variable state/ ρ -like class observations are shown in the upper and lower top right panels respectively. Bottom left panel : the time evolution of the characteristic oscillation frequencies in the variable state/ ρ -like class observations from both IGR J17091-3624 (hollow circles) and GRS 1915+105 (solid squares) are shown respectively. Bottom right panel : the plot of characteristic oscillation frequencies in the variable state/ ρ -like class observations as a function of the rms amplitude(%) of the characteristic pulsation is shown for both IGR J17091-3624 (hollow circles) and GRS 1915+105 (solid squares).

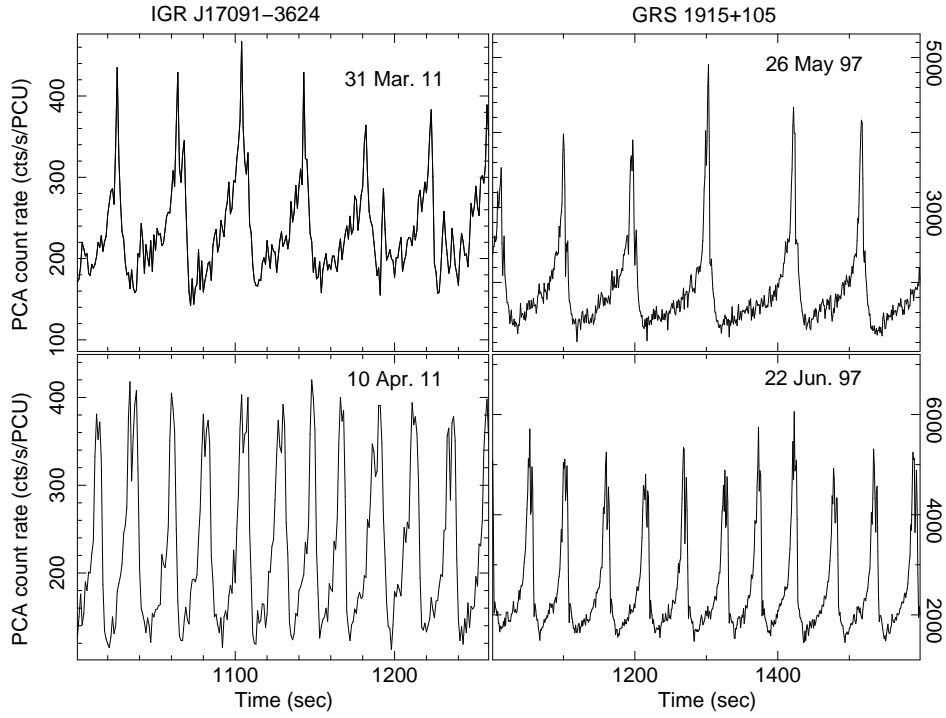


FIG. 7.— Comparative study between the variable state/ ρ -like class in IGR J17091–3624 and the ‘ ρ ’ class of GRS 1915+105. Left panel figures correspond to 2.0–60.0 keV *RXTE*/PCA light curve of IGR J17091–3624 on 31 March 11 (top) and 10 April 11 (bottom) and the right panel figures corresponds to 2.0–60.0 keV *RXTE*/PCA light curve of GRS 1915+105 on 26 May 97 (top) and 22 June 97 (bottom). A decrease in variability time scale with time is common to both sources as they evolve.

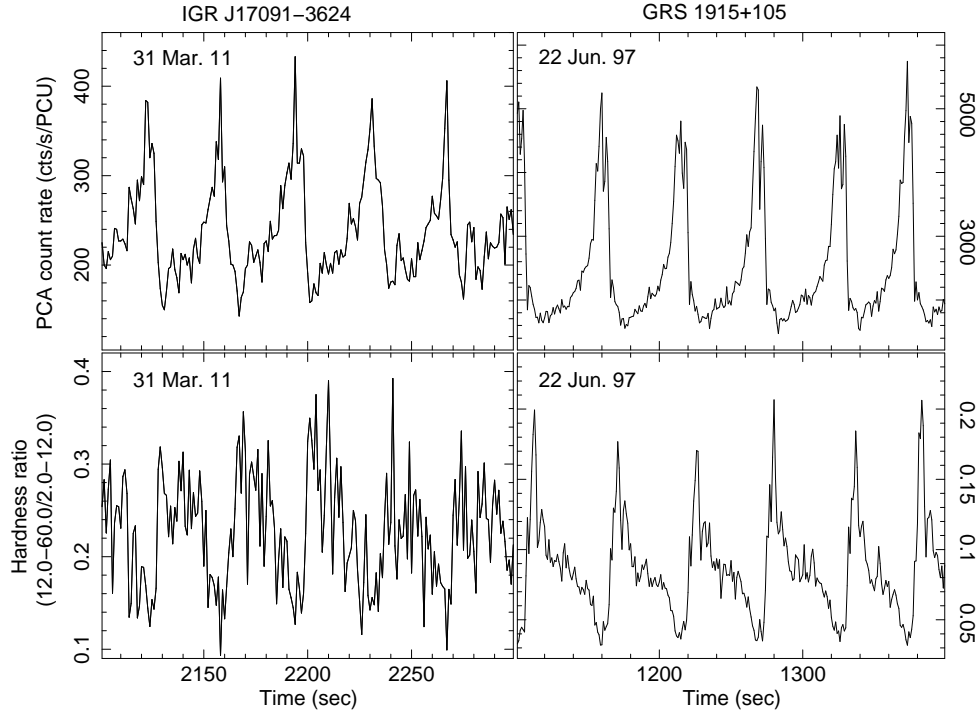


FIG. 8.— Comparative study between the variable state/ ρ -like class variability class of IGR J17091–3624 and the ‘ ρ ’ class of GRS 1915+105. Top panels show the 2.0–60.0 keV *RXTE*/PCA light curve of IGR J17091–3624 (left) and GRS 1915+105 (right). Bottom panels show the plot of hardness ratio (defined as the ratio of *RXTE*/PCA count rate between 12.0–60.0 keV and 2.0–12.0 keV) with time for IGR J17091–3624 (left) & GRS 1915+105 (right). Strong anti correlation between X-ray flux and hardness ratio is found in both sources.

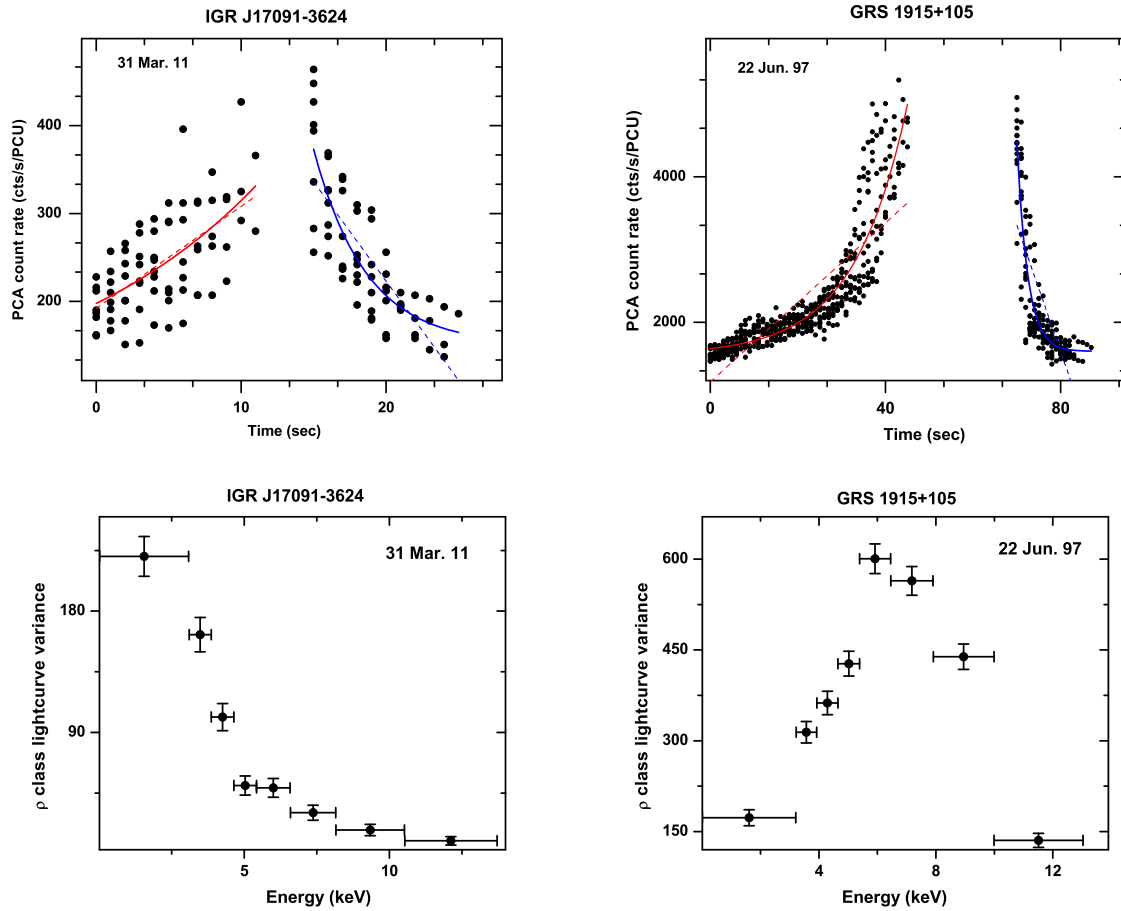


FIG. 9.— Comparative study between the variable state/ ρ -like class variability class of IGR J17091–3624 and the ‘ ρ ’ class of GRS 1915+105. *Top panels:* combined rise profile (left) and decay profile (right) of several bursts in IGR J17091–3624 (top left panel) and GRS 1915+105 (top right panel). Start of all rise profiles are normalized to 0 sec in both sources and start of all decay profiles are normalized to 15 sec in IGR J17091-3624 and 70 sec in GRS 1915+105. In both sources, an exponential growth function ($ae^{x/t}$) and an exponential decay function ($ae^{-x/t}$) (shown by solid lines) can fit the rise and decay profiles respectively, better than a straight line (shown by dotted line) with the significance $>3\sigma$. *Bottom panels* show the lightcurve variance spectra during ‘heartbeat’ oscillations in IGR J17091-3624 (bottom left panel) and GRS 1915+105 (bottom right panel). A discontinuity is observed in the spectra at ~ 6 keV in GRS 1915+105 whereas the variance spectra of IGR J17091-3624 is monotonous.

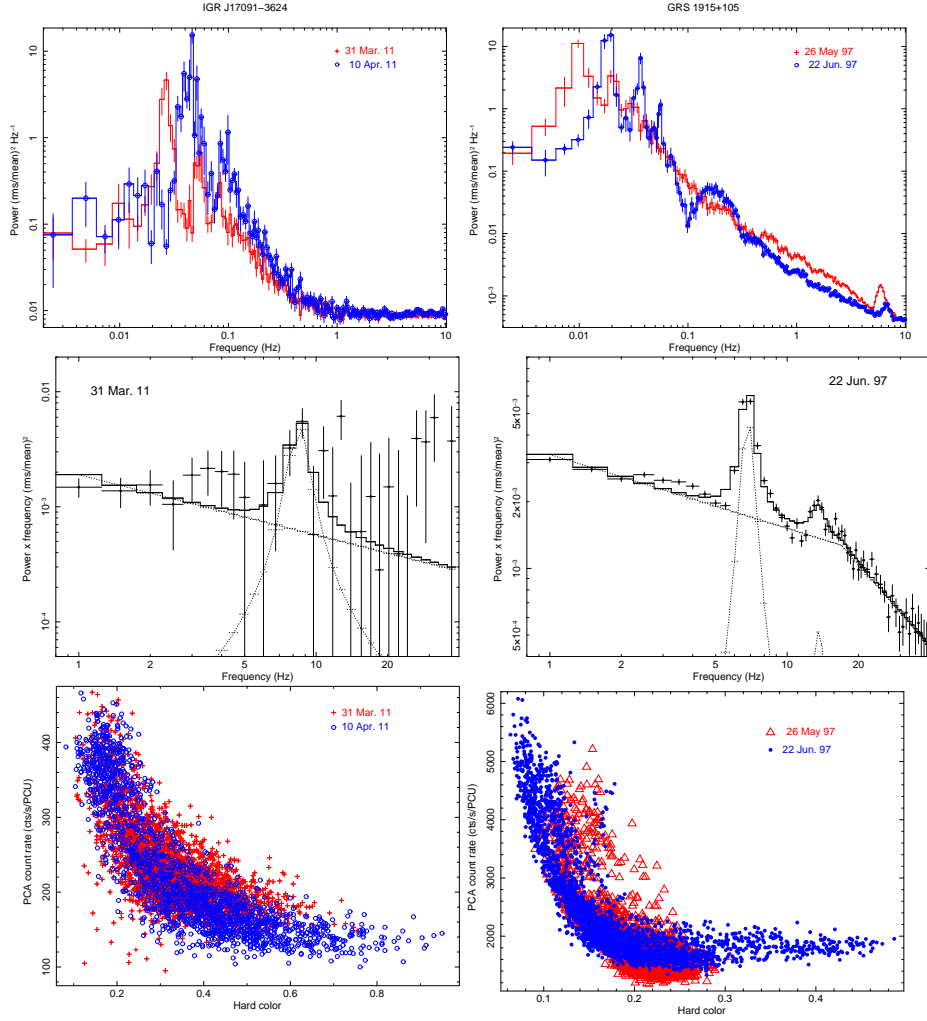


FIG. 10.— All left panel figures correspond to IGR J17091–3624 and all right panel figures correspond to GRS 1915+105. *Top panels:* 2.0–60.0 keV *RXTE*/PCA rms normalized power density spectra. *Middle panels:* Typical type-A 7–10 Hz QPO in the PDS of IGR J17091–3624 (middle left) and a type-B QPO in the PDS of GRS 1915+105 (middle right) during the variable state/ ρ class. *Lower panels:* Hardness Intensity Diagrams for the same definition of hard color and intensity. Both panels show that both sources evolved in a similar way in the PDS as well as in HIDs as the characteristic oscillation frequency changes.